DRAFT TECHNICAL DESIGN REPORT

for

@

(Dated: November 19, 2022)

The DarkLight@ARIEL Collaboration

Arizona State University, Tempe, AZ, USA

University of British Columbia, Canada

Hampton University, Hampton, VA, USA

TJNAF, Newport News, VA, USA

Massachusetts Institute of Technology, Cambridge, MA, USA

St. Mary's University, Halifax, Nova Scotia, Canada

Stony Brook University, NY, USA

TRIUMF, Vancouver, British Columbia, Canada

University of Manitoba, Canada

University of Winnipeg, Manitoba, Canada

CONTENTS

1. SCIENTIFIC MOTIVATION

The Standard Model (SM) describes the physical universe in terms of interactions between point-like fermions (quarks and leptons), gauge bosons which mediate those interactions, and the Higgs field that provides mass to the fermions. Combined with Einstein's theory of gravity (General Relativity), this theory, summarized in Fig. 1.1, has been incredibly successful. The vast majority of experiments have been consistent with the SM, and no

FIG. 1.1: Summary of the Standard Model of physics from [1].

credible alternatives have been put forth.

Notwithstanding its enormous success, we know that the SM is not the complete description of Nature. Firstly, more than two dozen parameters are put in by hand without any justification. More significantly, there are large open questions in our understanding of the universe that the SM fails to address. These include the asymmetry between matter and anti-matter and the origin of dark matter. Finally, there are laboratory experiments that report observations in significant tension with the SM.

This proposal is motivated by the observation of anomalies from low energy experiments. In particular, the ATOMKI experiment in Hungary reports anomalies in the electromagnetic

decays of excited states of the ^{4}He and ^{8}Be nuclei [2–4]. The experiment proposed here is motivated by the conviction that any reports of possible extensions beyond Fig. 1.1 must be independently validated with high priority.

1.1.   The Elusive Dark Matter

The search for an understanding of the elusive Dark Matter is one of the great scientific quests of our age. In the 1930s, astronomers first made determinations of the gravitational mass of galaxies that were significantly larger than expected from the observed luminosities and wrote of *dunkle Materie* [5]. Almost ninety years later, there is collective evidence that is substantial and consistent across seven orders of magnitude in distance scale (from about 1 kpc to 10 Gpc) that an unknown substance—dark matter—shapes the large-scale structure of the universe. We can infer a great deal from the gravitational effects of dark matter: We know the approximate density and velocity of dark matter in our galaxy, and that it does not form tightly bound systems larger than about 1,000 solar masses. It is also abundant, seeming to account for about 85% of the mass of the universe. In our current understanding, the known, uncharged particles, i.e. the neutron or neutrino, cannot be a major component of the inferred dark matter mass, and so we posit at least one as-yet unobserved new particle.

This particle must obviously interact gravitationally, but we expect it also interacts with the visible universe through other mechanisms, with coupling on the order of the weak interaction or less, in order for dark matter to be in equilibrium with other matter in the early universe.

The focus over several decades has been to look for a particular type of possible dark matter, a Weakly Interacting Massive Particle (WIMP), via a rare scattering from an atom in a large detector, typically located deep underground to minimize the rate of background events. The WIMP mass region explored by such experiments typically ranges from about 3 GeV to 10 TeV, and present experiments have probed WIMP-atom interaction cross sections lower than about 10^{-46} cm^2 at a WIMP mass of about 50 GeV. Thus far, no conclusive evidence for WIMPs has been found. Searches for WIMPs will continue for at least another decade. However, there is a fundamental floor on this approach due to the inability to distinguish

between a neutrino-atom interaction and a WIMP-atom interaction.

A complementary experimental thrust in the quest to understand dark matter is to search for evidence of the mediator of a new interaction between our visible world, successfully described in terms of four forces (gravity, electricity and magnetism, nuclear force and weak force), and the world of dark matter. This new interaction would constitute a fifth force. The simplest mediator widely considered is a dark photon, A', that couples to the known particles via their electric charges. The searches involve experiments using particle beams delivered by accelerators to produce the mediator. This mediator decays either into (a) known, detectable particles that are sought (*visible decays*) or (b) into dark-sector particles, which are undetectable, but whose presence is deduced by observation of a large missing energy and momentum in the final-state (*invisible decays*). The results of the searches are usually summarized in terms of their ability to constrain the mediator-to-known-matter coupling strength and the mediator mass. At the Large Hadron Collider at CERN, Geneva, Switzerland, searching for evidence of dark matter is a major activity at the collider experiments.

1.2.   A New Low Mass Mediator

Recently, there has been a focus on a mediator of a new fifth force, beyond the SM of Fig. 1.1, with mass lower than 1 GeV. Astrophysical observations and observed anomalies in measurements involving the muon and nuclear transitions, hint at this possibility. For example, the observed 3.5σ deviation between the measured and expected anomalous magnetic moment of the muon [6] can be explained by a fifth force with mass in the range 10 to 100 MeV [7]. There have been extensive searches for the dark photon, mainly through the study of π^0-decay in existing experiments, and much of the parameter space of coupling and mass that corresponds to these anomalies is excluded at 2σ [8]. However, a more general fifth force, where the couplings are no longer directly proportional to the electric charges, can not yet be ruled out.

It is straightforward to adjust the quark couplings of a fifth force to satisfy existing constraints and still allow such a force acting via lepton coupling to produce a signal. A number of recently-reported anomalies motivate further searches for such an effect at low energies:

Studies of the decays of an excited state of ^{8}Be to its ground state have found a 6.8σ anomaly in the opening angle and invariant mass distribution of e^+e^- pairs produced in these transitions [2], and a similar anomaly has recently been announced in ^{4}He [3, 4] (see Fig 1.2). While these discrepancies may be the result of as-yet-unidentified nuclear reactions or ex-
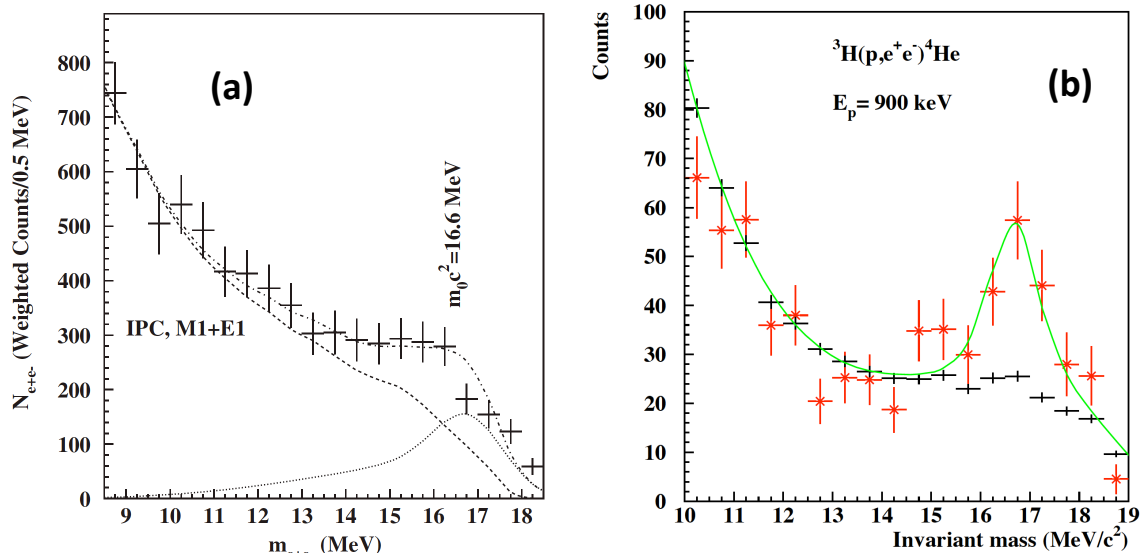

FIG. 1.2: (a): Anomaly in ^{8}Be [2]. (b): Anomaly in ^{4}He [4].

perimental effects, they can be simultaneously explained by the production of a new boson with a mass around 17 MeV. These results have attracted great attention in the popular media [9, 10], and urgently demand independent experimental verification. New bosons that couple atomic electrons with neutrons in the nucleus are also implicated in atomic physics experiments. The effect of this new interaction on energy levels and transition frequencies could be detected through precision isotope shift measurements. In particular, the scaled isotope shifts on two different transitions should exhibit a linear relationship (the so-called *King plot*). A deviation from linearity can be evidence of a new force mediator. Such deviations at the 3σ level have been reported [11] in the isotope shifts for five Yb$^+$ isotopes on two narrow optical quadrupole transitions $^2S_{1/2} \to {}^2D_{3/2} \to {}^2D_{5/2}$.

The focus of this proposal is to search for evidence of this possible new particle of mass around 17 MeV in e^+e^- final-states in electron scattering from a nuclear target.

1.3. Alternative Interpretations and Other Searches

The primary path to reconciling the ATOMKI anomalies with other searches that exclude dark photons in that region is to consider the couplings to quark and lepton flavors independently. Feng et al. demonstrated that u and d couplings that produce protophobic or nearly protophobic interactions would satisfy all contemporary limits[12]. In light of that observation, the X17 anomaly has been interpreted in various more specific theoretical models as a new particle, a Z', axion, or other light pseudoscalar [13–16].

There has also been some success in generating an X17-like angular correlation within the standard model through careful treatment of higher order effects. Zhang and Miller [17] suggest that form factor corrections can produce peaking structures in invariant mass, though it is not clear that this can produce the angular correlations seen in the ^{8}Be experiments, and the required form factor implies an anomalously large charge radius that is not expected from microscopic calculations. More recently, it has been demonstrated that interference between leading and next-to-leading terms in the internal pair creation matrix element can produce resonant structures in mass and angular correlations [18], and that such resonant structures can also arise from consideration of other nuclear states in the matrix element[19]. Some of these studies suggest that detector acceptance effects may enhance the size of such a peak beyond the Born-level shaping effects. These predictions could be checked experimentally, but, to our knowledge, no proposals to independently investigate ^{8}Be decays have advanced to operation.

We note a key indirect search of this parameter space, the Fermilab g-2 experiment, has recently released preliminary results in good agreement with the previous BNL measurement [20] (see Fig. 1.3). In the longer term, many experiments have been proposed, are under construction, or are currently taking data, that will directly search for dark photons through a variety of leptonic and hadronic channels. However, few can probe the mass and coupling range implied by the X17 anomalies in model-independent ways. Of those that can, LHCb, currently operating at CERN, has the shortest timeline. Upgrades currently underway are expected to extend the mass region it can reach in the subsequent run. The data collected 2021-2023 is expected to fully cover the X17 anomaly region[21]. Several other experiments will also have some sensitivity to this range in the coming decade.
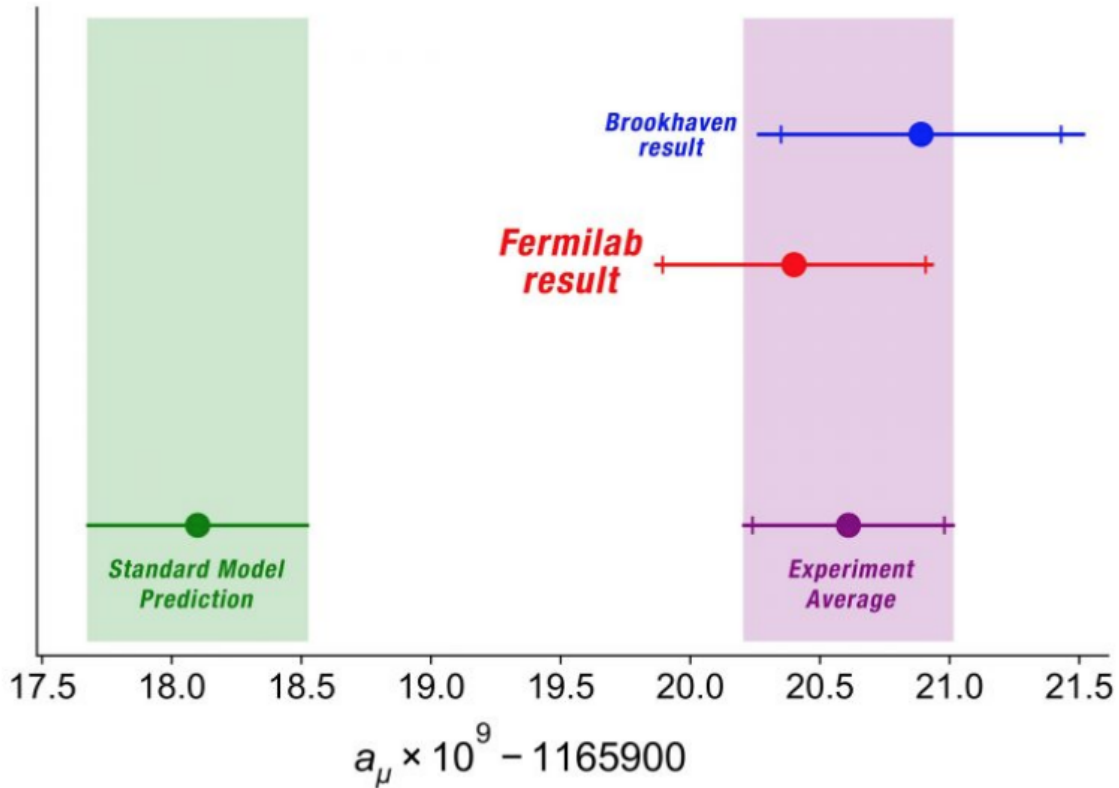
FIG. 1.3: The first result from the Muon g-2 experiment at Fermilab confirms the result from the experiment performed at Brookhaven National Lab two decades ago. Together, the two results show strong evidence that muons diverge from the Standard Model prediction.

LDMX, currently proposed and under development, will search primarily for decays using dark-QCD model assumptions [22], but has projected sensitivity, through displaced vertices, to model-independent couplings near the X17[23]. Although these would not rule out the current X17 allowed region in a model-independent way, evidence of the anomaly in these channels would be a strong confirmation. LDMX could begin data taking as early as 2023, and would expect a signficant data sample by 2025.

Belle-II can explore a large coupling space via J/Ψ decay, but due to the suppression of hadronic couplings in the X17 models, will not be able to directly probe the anomaly via that channel. It has been proposed to also search via displaced vertices [24], and projects that it can exhaust the remaining X17 parameter space with 50ab^{-1}, which it expects to

reach by 2027.

MAGIX (under construction for MESA, and scheduled to begin shortly after that accelerator is operation) will also be able to access this range [25], and could test the protophobic hypothesis with approximately six months of data at design luminosity.

Other experiments have suggested some sensitivity, but do not yet have clear projections. NA64, which in 2020 extended their analysis to exclude part of the X17 region, has stated that it will be difficult to extend the current exclusion with that approach [26]. The PADME experiment [27] could also potentially reach the X17 region, but would require some change to the experimental design. Details, and resulting sensitivity, are not yet available.

A search for the X17 via low-energy radiative production and leptonic decay would permit a nearly model-independent search of the allowed mass and coupling parameter space, avoiding possible nuclear effects. If mounted in the near future, any observed resonance could then be supported by complementary measurements in different channels and configurations from other experiments as they come online in the following years.

1.4. Fifth Force Parameter Space

The existing exclusions on the production of dark photons can be divided into measurements observing hadronic production mechanisms (e.g. π^0 decay) and those observing leptonic production mechanisms (e.g. e-p scattering, e^+e^- annihilation). In the simplest dark photon model, the effective coupling to a new force-carrier is proportional to electric charge, so all these exclusions apply to the same parameter space, but in more generic fifth-force models [12], this restriction is relaxed.

The wider parameter space has multiple couplings—most generally an independent coupling to each flavor of quark or lepton. Since these couplings are no longer directly linked, many of the experiments which probe the ^{8}Be anomaly region in the simplest dark photon model, and which depend on various hadronic couplings, no longer directly inform the coupling to electrons. Indeed, the $g-2$ and ^{8}Be anomalies suggest a particle whose coupling to some quark flavors is significantly suppressed, implying a substantially reduced sensitivity in some hadronic production modes.

The strongest remaining constraints on the electronic coupling near the ^{8}Be anomaly region come from measurements by NA64 [28] for small couplings, and from electron g-2 measurements for large couplings, with a key region of the anomaly region still untested (see Fig. 1.4). New results of NA64 [29] include a larger statistical sample and pushes the lower
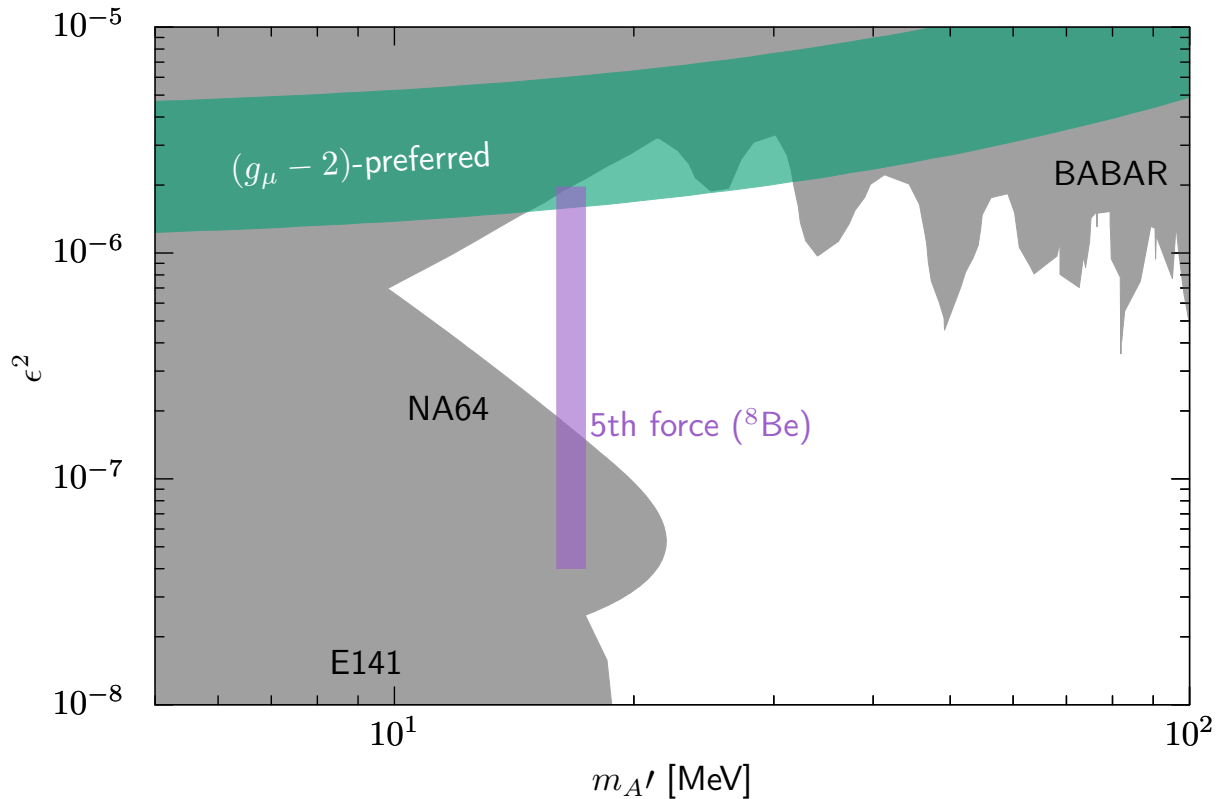

FIG. 1.4: Parameter space for a fifth force, with ^{8}Be and $g − 2$ anomalies in color. The vertical axis is the leptonic coupling strength relative to α_{QED}, with horizontal axis the mass of the mediator. Excluded regions, in gray, are taken from measurements that depend solely on leptonic interactions. In the general case, dark photon exclusions via hadronic measurements may be suppressed by large factors and so are not shown.

exclusion bound at the relevant mass up to $\epsilon^2 \approx 5 \times 10^{-7}$. First calculations indicate that the effect found in ^{4}He would be compatible with a similar coupling range.

A program to fully search the available parameter space for corroboration of the ^{8}Be anomaly will require both leptonic and hadronic probes: If a new particle is observed in one of these modes, it will be of utmost interest to measure all of its couplings. If it is not observed, both modes will be needed in order to definitively rule out the couplings required for the production of the new boson inside the nucleus and its prompt decay into electrons.

The LHCb collaboration has proposed an inclusive search for a dark photon in electron-positron pairs in LHC Run 3 (planned to complete data-taking in 2022) with sensitivity to a large region of the original A' parameter space. They also collected a smaller dataset in 2018 which contains tagged η and π^0 events with electron-positron pairs.

Purely leptonic searches that can be undertaken on similar time scales, like the one proposed here, will form the leptonic counterpart to hadronic experiments like LHCb, and clarify the interpretation of the latter's results by narrowing the range of allowed electron coupling.

2. EXPERIMENT

2.1. Overview

Motivated by the developments described above, we have designed an experiment to use the 30 MeV electron beam from the e-linac driver at ARIEL to search for new bosons with masses near 17 MeV.

The proposed experiment aims to measure the process $e^- Ta \rightarrow e^- TaA' \rightarrow e^- Ta(e^+e^-)$ looking for a resonant excess of e^+e^- pairs at the invariant mass of the A' around 17 MeV. The produced leptons are detected by a pair of dipole spectrometers arranged asymmetrically around a thin tantalum foil target placed in the beamline of the electron linac of ARIEL just upstream of the beamdump in the electron hall (see Fig. 2.1).

The use of the ARIEL e-linac has the benefit of allowing a relatively low beam energy, thus reducing the boost of a produced boson and opening up the small angles of these forward-going decay leptons. The experiment proposed here takes advantage of these larger angles. We propose a two spectrometer setup optimized for the anomaly region and using a thin foil target to achieve sufficient luminosities without blowing up the low energy beam excessively.
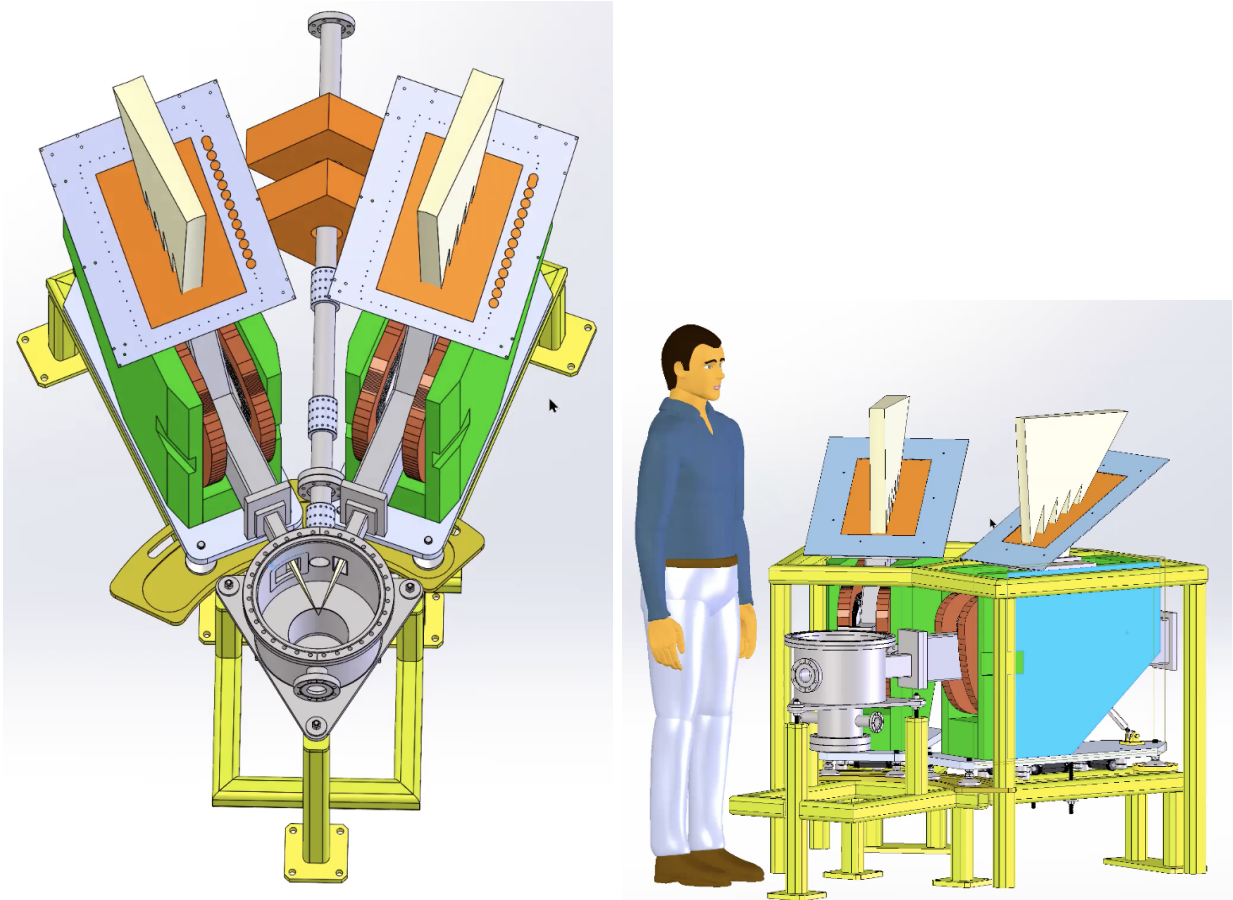
FIG. 2.1: CAD representation of the proposed experimental layout showing the scattering chamber, pair of magnetic spectrometers, and GEM focal plane detectors. Top and side views are shown.

2.2. ARIEL

TRIUMF's existing superconducting electron linac can currently produce an electron beam of up to 30 MeV in energy and peak intensities up 3 mA. As a driver of the Advanced Rare IsotopE Laboratory (ARIEL), the e-linac delivers electrons to a photo-converter target station for the production of neutron-rich rare isotope beams via photo-fission. Although the current e-linac license only permits operation up to 30 MeV of energy, it could potentially be possible to increase this to 31 MeV or higher with the current hardware following a re-evaluation of the licensing. Studies in the rest of this report assume 31 MeV beam energy unless otherwise specified.

Full access to the 17 MeV mass range requires a beam energy increase to 50 MeV. This can

be possible following alterations to the e-linac as discussed in the following three stages of experiment evolution.

Stage 0

> This would require very moderate modifications to the existing accelerator and the location will be in front of the existing 10kW dump, shown in Fig. 2.2. The electron beam energy would be 30 or up to 31 MeV. The linac would be operated in a continuous wave mode, with a bunch frequency of 650 MHz, and an average beam current of up to 300 μA.
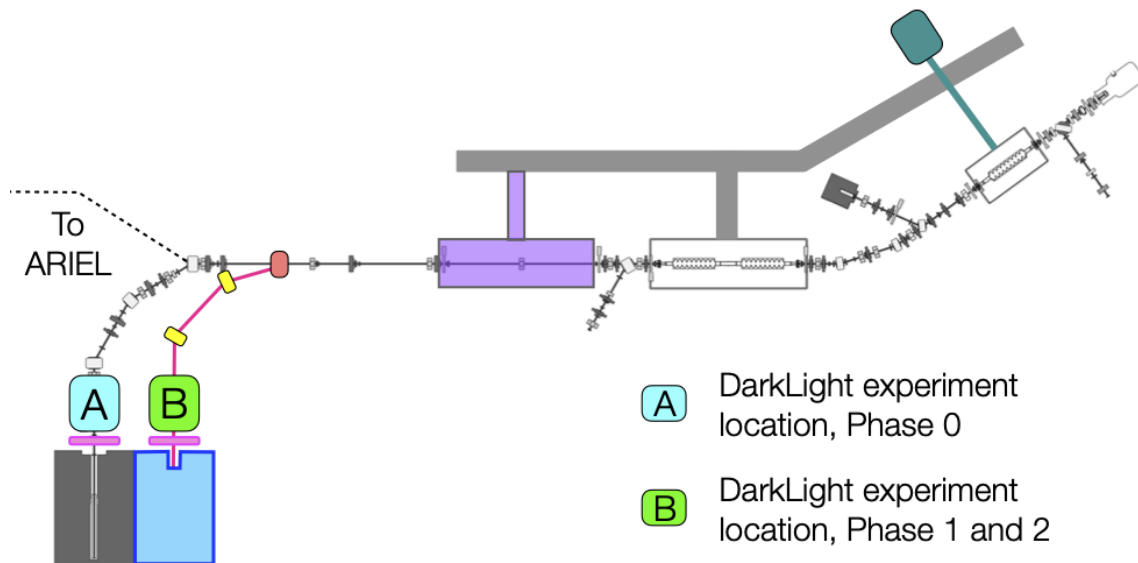

FIG. 2.2: Floorplan of the ARIEL e-Linac outlining the location of the 3 phases of the DarkLight experiment. For the first measurements at 30 MeV, the experiment will be placed in the area marked A. For 50 MeV beam, it will be moved to position B.

Stage 1

> Here a second cryomodule would be added to raise the beam energy to 50 MeV, as well as a new dedicated dump and beamline. The experiment would move in front of the new dump. This stage will run as a single user experiment with a dipole magnet deflecting the beam through the target into the new dump.

Stage 2

Here a septum magnet and RF deflector are added to allow for simultaneous 50 MeV beam delivery to ARIEL and DarkLight. Every other bunch would be sent through the Darklight target to the dump, and every other bunch would be sent to ARIEL.
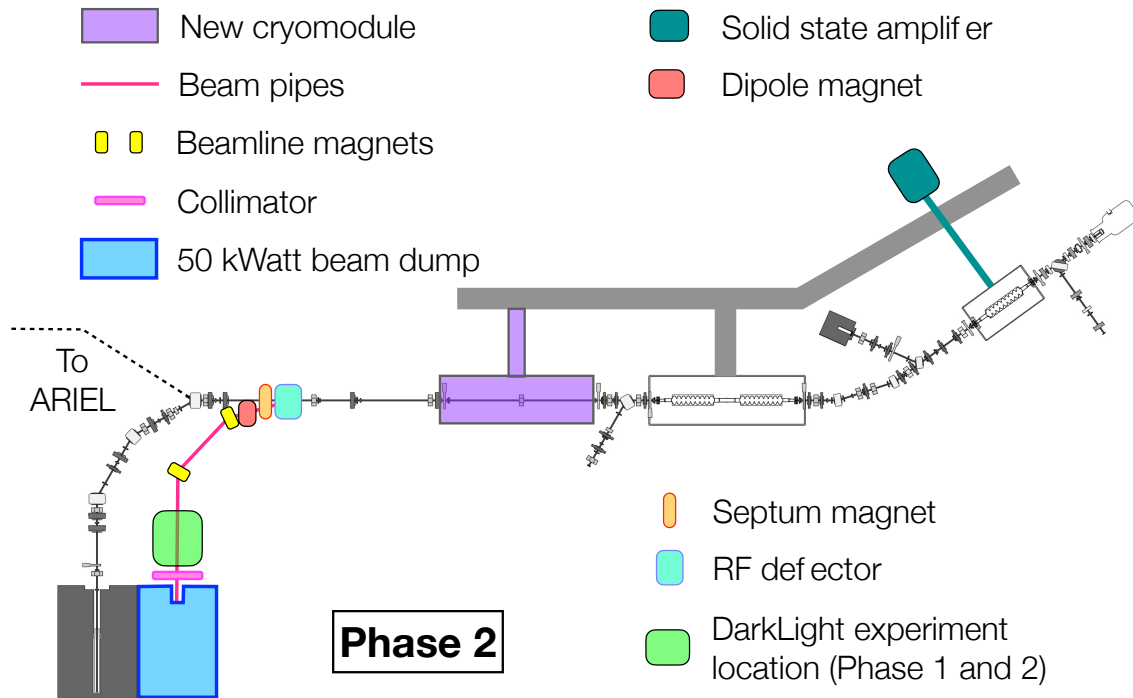

FIG. 2.3: Floorplan of the ARIEL e-Linac describing all the new elements needed for the final phase of the DarkLight experiment. The cryomodule allows the energy to be increased from 30 MeV to 50 MeV. The septum magnet and RF deflector enables concurrent beam delivery to ARIEL and DarkLight.

2.3. Beam Optics

Calculations and optimisation of the beam optics have been made at TRIUMF to ensure that the electron beam envelope remains inside the two inch diameter beampipe after the beam interacts with the tantalum target as shown in Fig. 2.4. The tantalum target (EACB:DL) is at s = 350 cm in the figure. Immediately after the scatering chamber are three, permanent magnet quadrupoles (PERMA1-3). These were chosen for their compact size allowing the
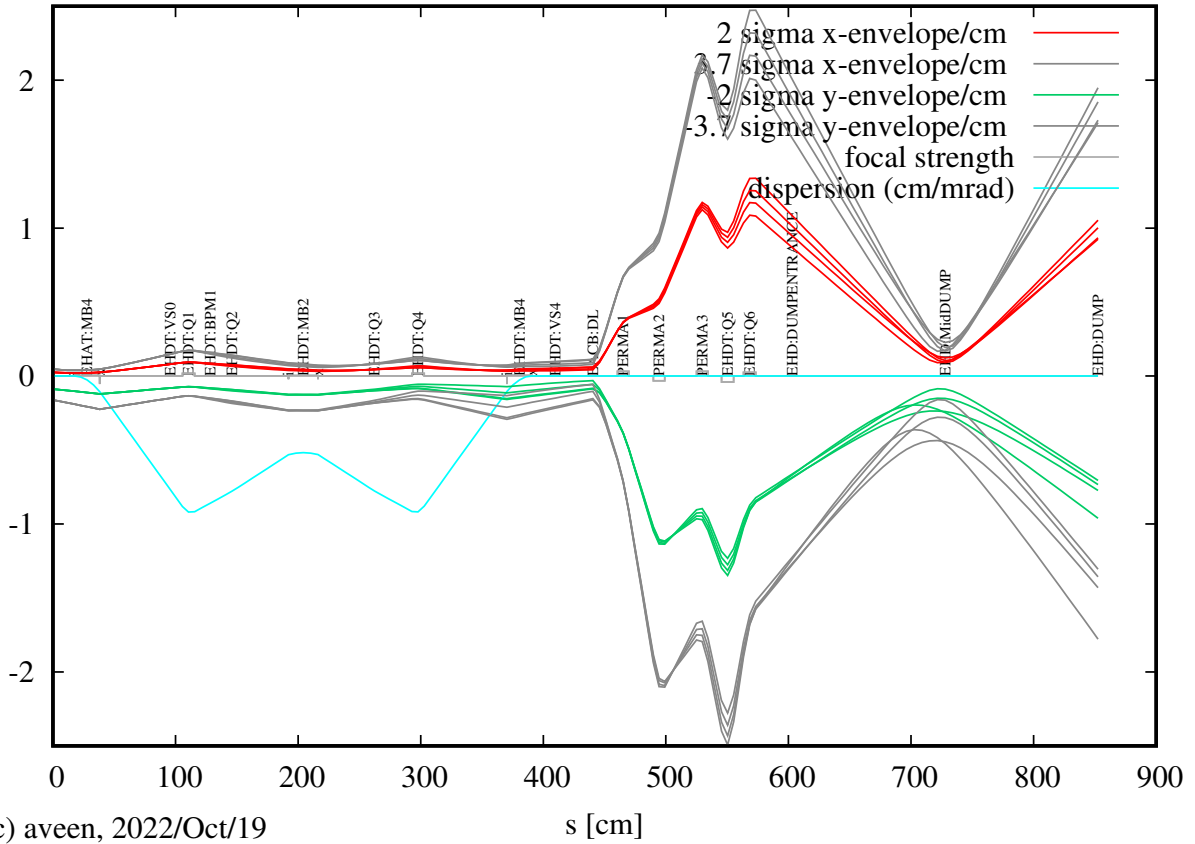
FIG. 2.4: Beam envelope representation showing that the horizontal and vertical beam
envelop and 3.7σ envelop remains inside the beampipe and into the beam dump.

spectrometer dipoles to approach the target and beamline as closely as possible. Another
pair of normal TRIUMF quadrupoles (EHDT:Q5-6) are used to finally focus the beam into
the centre of the beamdump. The entrance to the beam dump is around location s = 500 cm
and the mid-point is around s = 600 cm.

2.4. Target

The experimental design assumes a $31\,\text{MeV}$ e^- beam of $150\,\mu\text{A}$ on a $1\,\mu\text{m}$ tantalum foil. [46]
This produces an instantaneous luminosity of $\mathcal{L} = 5.2\,\text{nb}^{-1}\,\text{s}^{-1}$, i.e., $0.0275\,\text{fb}^{-1}\,\text{s}^{-1}$ hydrogen
equivalent, and will cause a beam spread of approximately $0.5°$ downstream of the target.
The beam will deposit about $0.4\,\text{W}$ in the target, which can be dissipated via radiation and
conduction to the target ladder frame for practical beam spot sizes (see Sec. B). Properties
of tantalum are provided in Table 2.1.

TABLE 2.1: Properties of tantalum.

atomic number (Z)	73
atomic mass (A)	181
density (g/cm^3)	16.65
radiation length X_0 (cm)	0.4094

The target ladder will also carry a 0.5 µm thick tantalum foil and a BeO screen. The thinner target would reduce beam blowup even further if necessary and the screen can be viewed by a camera to verify the beamspot size at the target location.

2.4.1. Beam Interaction with the Target

The 31 MeV electron beam loses energy and multiple scatters in the 1 μm thick tantalum target. The energy loss causes heating of the target and the multiple scattering increases the emittance of the beam and results in a growing beam size downstream of the target as it makes its way to the beamdump.

Energy Loss in the Target

The energy loss for an electron traveling through tantalum vs. energy is shown in Fig. 2.5. Radiation dominates over collisional processes at 31 MeV. Thus, each 31 MeV electron in passing through the 1 μm target loses on average

$$8 \text{ MeV}/(\text{g/cm}^2) \cdot 16.6 \text{ g/cm}^3 \cdot 10^{-4} \text{ cm} = 13.3 \text{ keV} \ ,$$

principally through radiation of bremsstrahlung.

Bremsstrahlung in the Target

The bremsstrahlung production by 31 MeV electrons in tungsten ($Z = 74$, $A = 184$) has been previously studied [33]. The photons produced are very forward peaked in angle and have an energy distribution that is dominated by $E_\gamma < 15$ MeV, as shown in Fig. 2.6. The highest energy photons go forward directly to the beam dump. It can be expected that
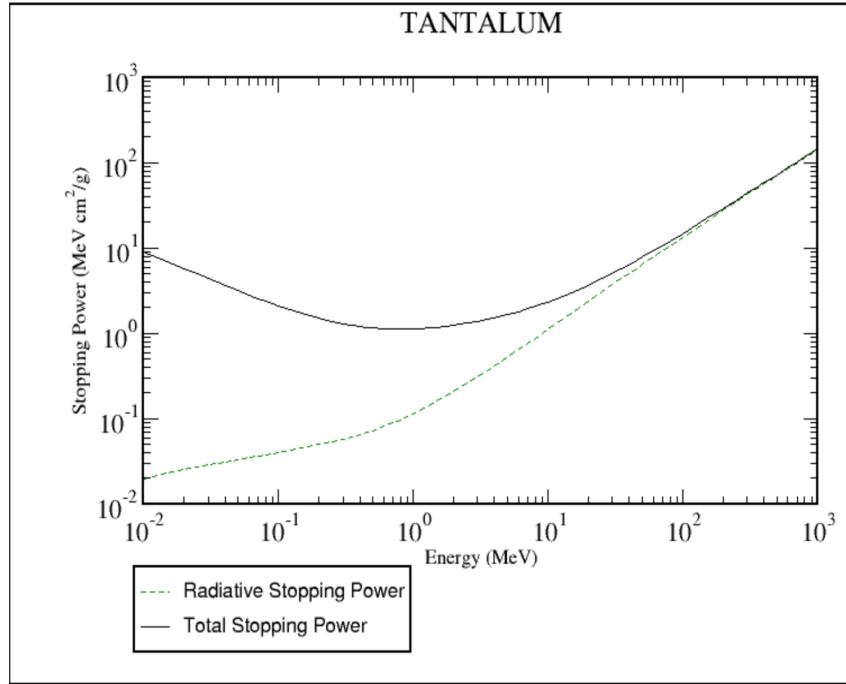
FIG. 2.5: The stopping power of electrons in tantalum vs. energy, from [32].

some photons of ∼MeV energy do scatter to the vicinity of the focal plane detector. Thus, it is prudent to incorporate effective shielding for MeV γ-rays around the detector. 4 cm of lead reduces the flux of 1 MeV photons by an order of magnitude so the mechanical support system will be designed to allow shielding of this thickness around the focal plane detector.

Neutron Production in the Target

Neutrons can be produced by electron beams through photonuclear reactions [34]. The total neutron production is composed of two parts: (1) photonuclear reactions via bremsstrahlung, and (2) electroproduction via virtual photons. In general, the cross section for electroproduction is expected to be of the order of the fine structure constant, $\alpha = 1/137$, times the cross section for the photonuclear reaction. The neutron yield produced by electroproduction becomes important when the target is thin, and the bremsstrahlung yield is low.

Giant Dipole Resonance (GDR) neutrons are produced by photons with energies from ap-
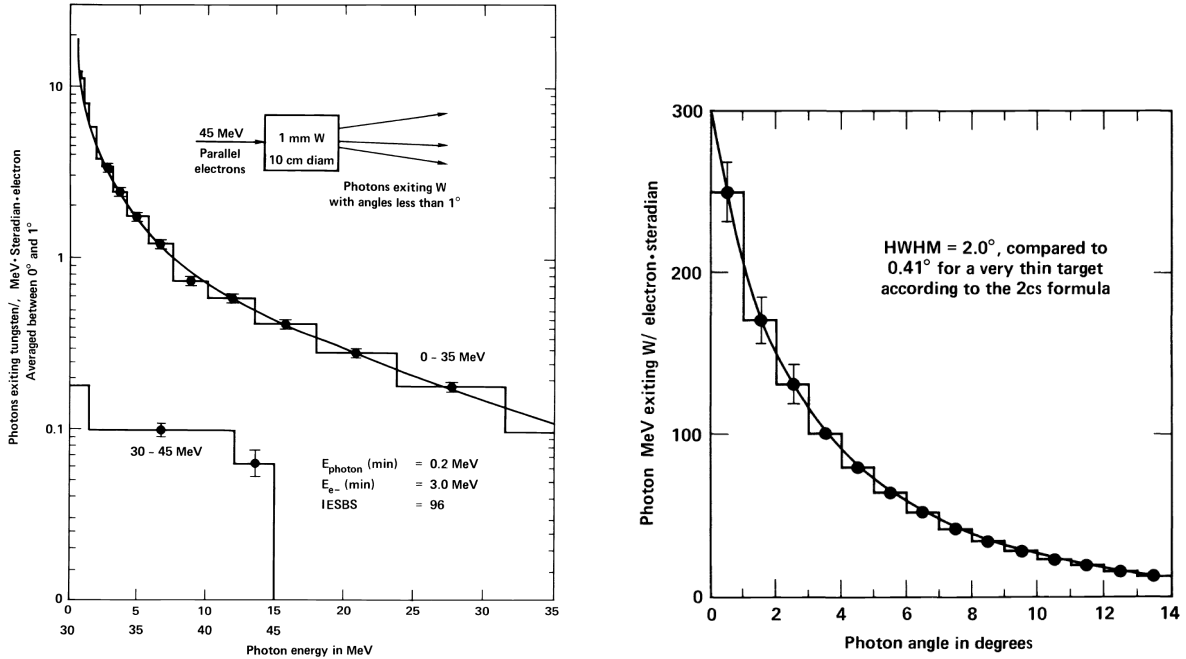
FIG. 2.6: Left: Bremsstrahlung spectrum of photons within $1°$ of the beam direction for 45 MeV electrons on 1 mm thick tungsten target from [33]. Right : Angular distribution of photons for 45 MeV electrons on 1 mm thick tungsten target from [33].

proximately 7 to 30 MeV. Neutrons from the photon-induced GDR reaction consist of a large portion of evaporation neutrons which dominate at low energies ($< 1-2$ MeV) and a small fraction of direct neutrons which dominate at high energies, as illustrated in Fig. 2.7. The GDR neutron yields are proportional to the product of the length l of the material traversed by photons of each energy (the photon track length) and the GDR photoneutron cross section. The dependence of the photon track-length on the photon energy k is expressed as the differential photon track length dl/dk, representing the total track length of all photons with energies in the interval $(k, k + dk)$.

In thin targets, neutrons produced by the direct interaction of electrons with nuclei may become important. The differential photon track length in thin targets must include an electroproduction (i.e., virtual photon) part:

$$\left(\frac{dl}{dk}\right)_{thin} = \left(\frac{dl}{dk}\right)_{brem} + \left(\frac{dl}{dk}\right)_{virtual} .$$

The total neutron yield produced by both bremsstrahlung and direct electroproduction in
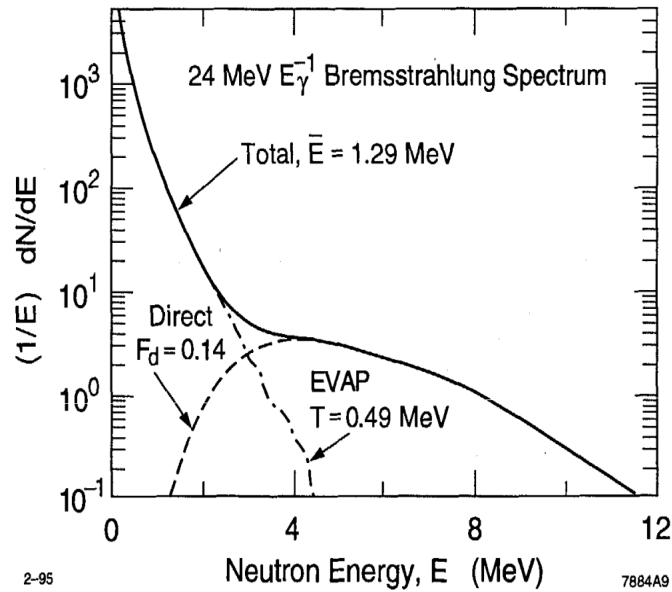
FIG. 2.7: Calculated photoneutrons from a tungsten target bombarded by a E_γ^{-1} bremsstrahlung beam with an endpoint of 24 MeV from [35].

thin targets is given by [34]

$$Y_{thin}^{total} = 8 \times 10^{-4} \times (1 + 0.12Z - 0.001Z^2) \times \frac{T^2}{E_0} \left(1 + \frac{0.04}{T}\right) \text{ neutrons/electron/MeV} , \quad (2.4.1)$$

where T is the target thickness in radiation lengths and E_0 is the electron beam energy in MeV.

For the proposed experiment with 9×10^{14} electrons/sec incident on the target

$$E_0 = 31 \text{ MeV}$$

$$T = 0.0024$$

$$Z = 73 \quad ,$$

we have a neutron production rate in the target of 8×10^{-9} neutrons/electron/MeV. With $I = 150$ μA, the neutron production rate in the target is 7.2×10^6 neutrons/s/MeV. The angular distribution of photoneutrons is assumed to be largely isotropic for evaporation neutrons while it is forward peaked with a $\sin^2 \theta$ distribution for direct emission. The average energies of the neutrons are a few MeV.
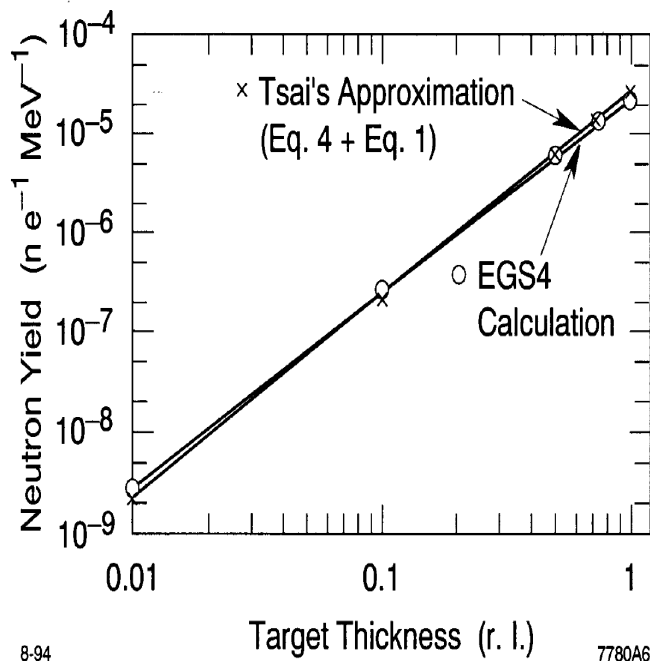
FIG. 2.8: Neutron yields produced by bremsstrahlung in thin iron targets struck by 100
MeV electrons as a function of the target thickness from [34].

Shielding neutrons involves three steps:

- Slow the neutrons to thermal energies (usually with hydrogenous material). Polyethy-
  lene, $(CH_2)n$, is a very effective neutron shield because of its hydrogen content (14%
  by weight) and its density (≈ 0.92 g cm^{-3}).

- Absorb the neutrons. Thermal neutrons can be captured through the ^{1}H$(n,\gamma)^2$H re-
  action which has a cross section of 0.33 barn for neutrons in thermal equilibrium at
  room temperature ($E_n = 0.027$ eV).

- Absorb the γ-rays. The emitted γ-ray has an energy of 2.2 MeV that provides a
  somewhat troublesome source of radiation exposure in some situations. The addition
  of boron can reduce the buildup of 2.2 MeV photons released in the thermal neutron
  capture by hydrogen by instead capturing the thermal neutrons in the boron, by means
  of the ^{10}B$(n,\alpha)^7$Li reaction. The latter has a cross section for "room temperature"
  neutrons of 3837 barns. In 94 per cent of these captures, the emitted α-particle is
  accompanied by a 0.48 MeV γ-ray. The α-particle is readily absorbed by ionization

while the γ-ray has a much shorter attenuation length than does a 2.2 MeV γ-ray. Commercially, polyethylene is available that includes additives of boron (up to 32%), lithium (up to 10%) and lead (up to 80%) in various forms such as planer sheets, spheres, and cylinders.

For example, 3.8 inch thickness of borated polyethylene reduces the flux of 1 MeV neutrons by an order of magnitude.

With a modest mix of borated polyethylene and lead shielding around both the target chamber and the focal plane detector, and taking into account the solid angle of the detector subtended at the target, this neutron rate can be decreased by at least three orders of magnitude. Further, the efficiency of the trigger scintillators for neutron detection is $< 1\%$ so that the background rate in the detectors due to neutrons produced in the target is $<$ 100 Hz, which is not a problem.

Multiple Scattering in the Target

From [38], we have the rms width in the angular distribution due to multiple scattering

$$\theta_{MS} = \frac{13.6 \text{ MeV/c}}{\beta p} z \sqrt{\frac{x}{X_0}} \ ,$$

where p, βc, and z are the momentum, velocity, and charge number of the incident particle, and x/X_0 is the material thickness in radiation lengths. For the 31 MeV beam on the 10 μm thick tantalum target, $\theta_{MS} = 15$ mrad.

The beam emittance is increased by $\sim \pi \times 15\text{mrad} \times 300\mu\text{m} = 0.01$ nm$-$rad, which is negligible compared to (1) and (2) above. However, the 15 mrad multiple scattering angle will cause the beam radius to increase by 15 mm per meter of travel downstream of the target. 3 meters of travel will result in a beam of diameter ~ 4 inches, which requires that the beampipe diameter be large enough to accommodate this.

2.5.   Spectrometers

The experiment will make use of two dipole spectrometers, with very similar magnetic characteristics, under design and to be built by MIT (see Fig.2.1). The spectrometer design is

similar to that of the spectrometer previously constructed for the radiative Møller scattering measurement with point-to-parallel focusing in the non-bend plane to get better resolution in the non-bend plane angle. For each spectrometer, the solid angle acceptance is 12 msr, and the momentum acceptance is ±20%. Both spectrometers will be designed to the same specifications, presented in Table 2.2.

TABLE 2.2: Design parameters for the spectrometers.

In-plane acceptance	$\pm 2°$
Out-of-plane acceptance	$\pm 5°$
Momentum acceptance	$\pm 20\,\%$
Minimum central angle	$16°$
Maximum central momentum	$28\,\mathrm{MeV}$
Dipole field	$0.32\,\mathrm{T}$
Nominal bend radius	$30\,\mathrm{cm}$
Pole gap	$4\,\mathrm{cm}$

An initial conceptual design of the spectrometers has been completed, demonstrating that the desired features are readily achievable (see Fig. 2.9). The two spectrometers will be operated at different currents to produce the desired magnetic fields, but share a common magnet design. They are conventional iron-core magnets with simple, planar coils. The magnet design and pole face rotations were optimized for a 0.5 m distance from target to spectrometer entrance and for post-magnet trajectories suitable for tracking with 40 cm long GEMs. The final engineering of the magnet will include detailed design optimization to increase magnetic performance, minimize size, and maximize clearance to the exit beamline. The magnet in its present configuration weighs about 950 kg. The magnets will have full fiducialization to allow for laser tracking alignment and a six-strut mechanical support system to allow for 200 µm alignment (similar to other MIT-Bates designs). We are currently in the process of finalizing a full design as the basis for generating a simulated field map to verify and optimize the achievable resolutions. The electrical needs of the spectrometer are modest, 20 A at 40 V (under a kilowatt). Air cooling is used in the present configuration.
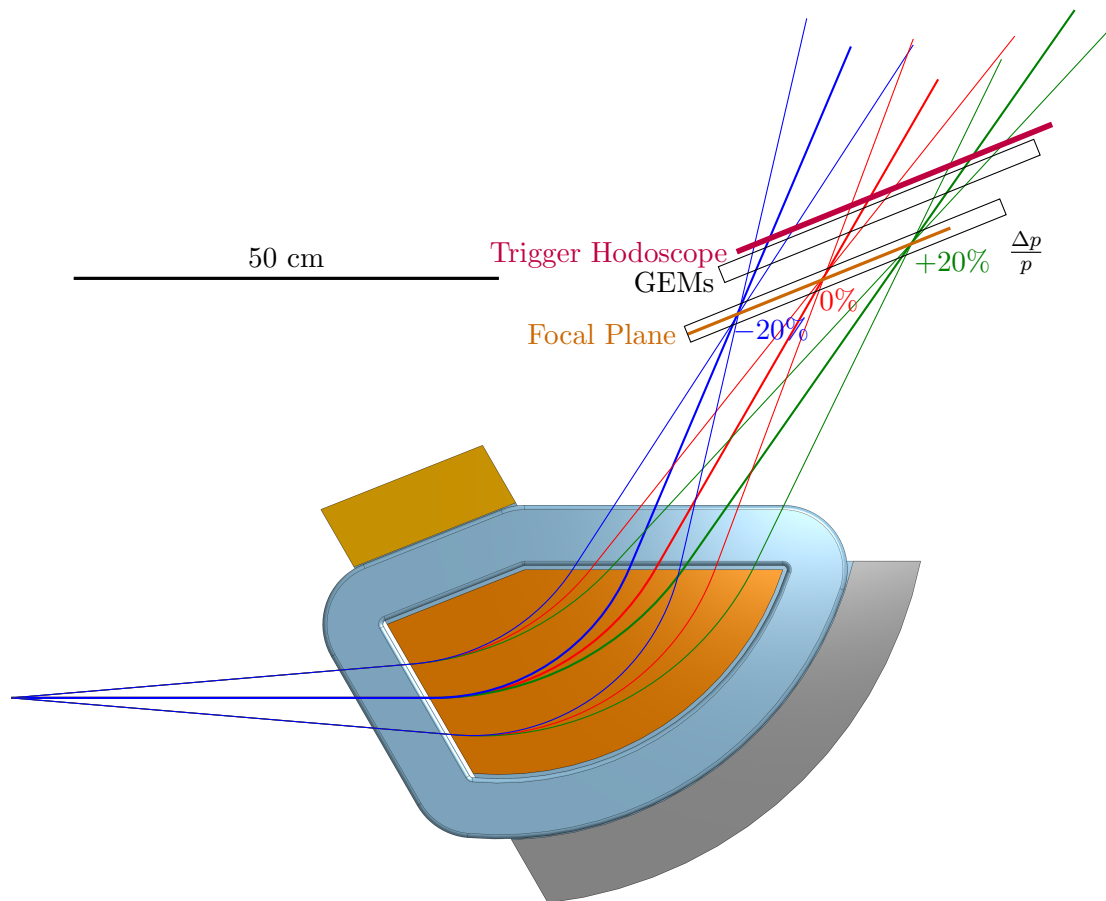
FIG. 2.9: Schematic overview of the spectrometer optics and detector package. Red is the central momentum p_0, with blue and green corresponding to $p_0 - 20\%$ and $p_0 + 20\%$, respectively.

2.5.1.   *Magnetic Field Measurement*

There are no plans to continuously monitor the magnetic field strengths of the dipole magnets during the course of the experiment. It is felt that monitoring the current output of the power supplies, together with the field maps of the dipole magnets, will be sufficient. However, the current output of a power supply is normally given by the voltage drop across a shunt resistor, which is potentially vulnerable to temperature change of the resistor as well as physical deterioration of the resistor. A secondary means of measuring the current could be provided by a CTR (current transformer). It would be prudent to, from time to time, measure the magnetic field strength, by a NMR or Hall probe. This should be placed in the uniform region of the field, as measurements in a fringe field are vulnerable to small changes

in the position of the probe. The experiment requires the magnetic field to be stable to one part in 10^3 which should be easy to establish by monitoring the current. Current probes and magnetic field probes are sold by GMW Associates.

2.6. Detectors

2.6.1. Trigger Hodoscopes

The standard GEM readout requires a trigger signal, to be generated from the coincidence of two fast trigger detectors in the spectrometers. To reduce accidental coincidences in the trigger logic, it is important to resolve the beam bunch clock of 650 MHz, at least at the analysis level. This timing information must be provided by the trigger detector, but can be corrected for the particle path length reconstructed from the tracking detector information. However, to reduce the readout dead-time, it is important to be close to the ideal timing during data-taking. The main time dispersion is generated by the momentum-dependent dispersion inside the spectrometers. We therefore propose a trigger detector made from scintillator paddles, divided along the dispersive direction into 8 segments, each read out via 6 SiPMs (3mm x 3mm Hamamatsu S13360-3075PE). These segments can then be timed in individually.

The scintillator paddles will be made from a standard plastic scintillator material (BC-404) and have a size of 150 x 38 x 3 mm^3.

2.6.2. GEM detectors

Each spectrometer will be instrumented with an identical tracking detector system consisting of triple-GEM elements. Eight such triple-GEMs have been designed and built by the Hampton group with funding from an NSF MRI award and are being commissioned as of Spring 2021.

With an active area of 25x40 cm^2 the GEM detectors cover ten times more area than the 10x10 cm^2 GEMs used in the 2016 prototype detector[47]. The intermediate size makes the envisioned set of GEM chambers also attractive for further use in other setups.

The GEM chambers have been built as triple-GEM detectors with a standard two-dimensional readout structure with 400 μm pitch between strips. The front-end electronics are based on APV front-end cards and Multi-Purpose Digitizers (MPD) of the latest generation (APV4.1 and MPD4.0), very similar to the system used previously at OLYMPUS and DarkLight Phase-1a, and presently at MUSE. The construction follows the so called NS2 scheme, and it is the first implementation for a GEM detector optimized for low-energy nuclear physics. More details can be found in appendix A. A system of GEMs+APVs+MPDs has recently been mass-produced at a larger scale for the Super-Bigbite Spectrometer (SBS) construction at Jefferson Lab.

Five triple GEM detectors suitable for DarkLight at ARIEL are available at Hampton University and can be commissioned using a Sr^{90} source and cosmic ray test stand. A further three detectors could also be returned from Japan if necessary.

2.7. DAQ, trigger electronics and slow control

The 6 signals from each end of the trigger hodoscope counters will be preamplified and then summed before being discriminated and timed (both leading-edge and trailing-edge) by a FPGA-based TDC. The firmware of the FPGA will allow us to generate triggers from e^+-e^- coincidences in very small coincidence windows, typically not possible with off-the-shelf coincidence units. The time-over-threshold will be used to make time-walk corrections to improve the overall time resolution. The small coincidence time windows are required to identify coincidences on the level of individual bunches,thereby minimizing the recorded background. The FPGA will also allow us to easily adjust the timing of individual trigger paddles, since the particle path length through the spectrometer, and thus, the time offset from the vertex, depends on the momentum.

The GEMs will be read out via APV25 ASICS and MPD4 readout boards provided by the Hampton group. We envision a VME crate per spectrometer to house the MPD4 and CFDs and the FPGA trigger module.

The required FPGA trigger firmware and basic DAQ software, as well as required slow controls will be developed by the TRIUMF DAQ group along with SBU. At the present

time we are planning to use the Chrono board that TRIUMF is currently developing for the DarkSide collaboration.

2.8.   Shielding

In addition to the shielding issues presented in the section on the Target (Sec. 2 2.4) there is a significant background electromagnetic radiation rate generated by the ARIEL RF cavities even if the beam current is zero. Field emmission in the cavities produces low energy electrons which can be accelerated by the RF cavities. These then strike beamline elements and produce high background rates in the electron hall. Recent tests showed rates on the order of several hundreds of kHz even when the detectors were screened from the RF cavities directly by concrete shielding blocks and lead bricks. The rate was proportional to the cavity high voltage increasing as the HV was increased to the design value for 30 MeV. This background is mostly low energy X-rays and the shielding outlined previously in Sec. 2 2.4 should be sufficient here as well.

In any case a detailed shielding plan will need to be devised and adequate support for the shielding incorporated into the design of the scattering chamber and detector packages.

2.8.1.   Experience with 100 MeV LERF Beam

The DarkLight collaboration carried out an important set of beam studies at the Jefferson Lab FEL/LERF in July 2012 [39, 40] which relate to the discussion of backgrounds at the experiment proposed here at the CEBAF Injector. Electron beam of energy 100 MeV and intensity 4.2 mA was passed through an aluminum block with apertures of diameter 6 mm, 4 mm and 2 mm and of length 127 mm. The main conclusion of the July 2012 run was that a 0.4 Megawatt electron beam of energy 100 MeV could be passed through a 2 mm diameter aperture with loses of 3 ppm for a duration of eight hours, thus establishing the feasibility of the DarkLight experiment. The interaction of beam halo with the block was measured through the rise in temperature of the block while simultaneously the photon and neutron backgrounds were measured with detectors in the vicinity of the block. The temperature and radiation measurements were consistent with simulations of the interaction [41]. The neutron production mechanism was via the Giant Dipole Resonance, as is the case for

the experiment proposed here. Fig. 2.10 shows the measured photon and neutron radiation levels during the eight-hour run. The fact that the measurements at 100 MeV were successful and the measured backgrounds consistent with the calculations, gives confidence that the background estimations here are reliable.
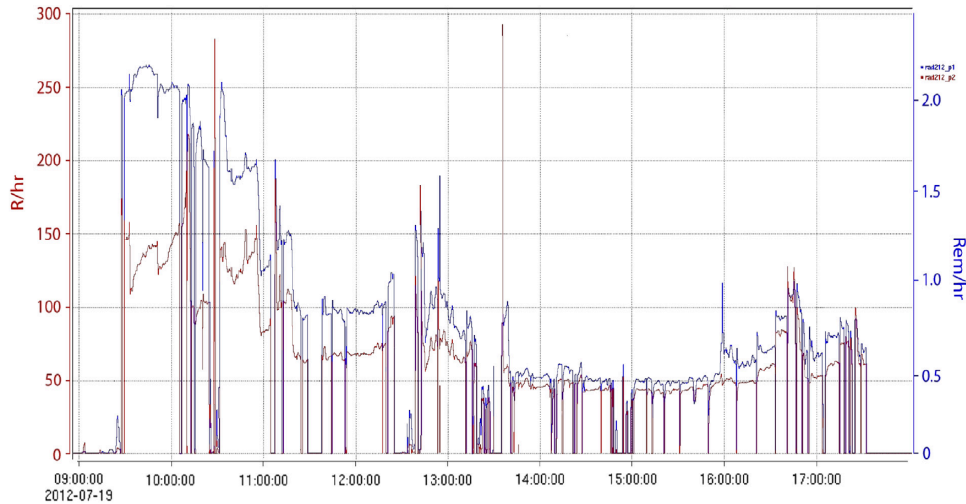

FIG. 2.10: Photon (darker trace, left axis) and neutron (lighter trace, right axis) radiation levels during the run with 4.2 mA and 100 MeV beam from the FEL [41].

3.   SIMULATION AND SOFTWARE

The eventual goal for a DarkLight software framework is to be able to:

1. Produce signal and background simulated samples containing both "true" particle trajectories and simulated output GEM hits inclusive of resolution effects and matching the output formats from the real detector

2. Reconstruct real and simulated hits into particle trajectories with one piece of code

3. Calculate uncertainties and perform a robust statistical analysis of the data.

The current plan is to fulfil these requirements using the following packages:

a.   Particle generation   To obtain high-statistics samples within the limited experimental acceptance, two dedicated generators are used.

- The Mainz generator [30] is used to calculate the cross section for $ep \rightarrow ep\gamma^* \rightarrow epl^+l^-$

at leading order with all leading order radiative corrections. The production of an A' signal decaying to a lepton pair is kinematically indistinguishable from the production of a γ^* with the same effective mass. The Mainz generator can therefore be used to generate both signal samples and irreducible background samples. For signal samples, γ^* events are generated in a very narrow mass window around the A' mass of interest, and only for leading order diagrams wherein a virtual photon directly decays to an l^+l^- pair. The cross section is normalised to that of a dark photon by a scale factor dependent on the kinetic mixing ϵ. For background estimation, the same generation takes place, but all leading-order diagrams are included, the γ^* mass is not restricted, and the cross section needs no rescaling. Note that using γ^* production to stand in for dark photons is an established method [45].

- The generator developed for OLYMPUS [31] is used to generate electrons which, after scattering in the target, radiate a hard photon and lose sufficient energy to enter the electron spectrometer acceptance. As with the Mainz generator, the outgoing particles are placed within the detector acceptance, and the cross sections for the relevant event then computed. The radiative cross section calculation uses the Bethe-Heitler approximation for photon radiation from the electron and the Born approximation for photon radiation from the proton, and includes additional tail corrections. [KP: I think.]

Both of the above generators should nonetheless be cross-checked, in so far as possible given the limitations of other generators, to ensure that the processes are well modeled and the cross sections accurate.

b. Detector simulation and reconstruction   Here a model of the target, spectrometers, and GEMs in GEANT4 will be used to propagate particle tracks from the generators through the relevant detector components, taking into account the magnetic field details as well as multiple scattering effects. The digitization process must take into account the efficiencies and resolutions of the real detector components to produce a realistic output. Particle tracks will be reconstructed using hits from simulation and the predicted magnetic field map.

c. Statistical analysis   The statistical framework can be easily constructed in pyhf, which allows for sophisticated handling of systematic uncertainties and simple computation of HEP-standard test statistics and exclusion limits.

The following sections describe the results of simulation-based studies completed thus far. All studies shown assume a 150 μA current.

3.1. Expected resolutions

We analyzed a first draft design for a magnet system in terms of resolution. For this, a magnetic field map was calculated via ANSYS Maxwell, then integrated into a GEANT4 simulation. In a first step, we traced particles through the magnet system without scattering in target and detector package to determine the simulated focal plane. We placed the virtual detector package with the first detector plane in the focal plane and a second plane 8 cm higher.

Assuming perfect resolution in the detector planes, we can now find the transfer function of the magnetic system: The detector system measures focal plane coordinates x (dispersive) and y (non-dispersive) as well as slopes dx and dy. We can find a series of function $f(x, y, dx, dy)$ to calculate the target parameters Θ (out-of-plane) Φ (in-plane) and p. We parametrize the function as a polynomial:

$$f_i = \sum_{a,b,c,d} \alpha_{a,b,c,d} x^a \cdot y^b \cdot dx^c \cdot dy^d$$

We find the parameters $\alpha_{a,b,c,d}$ using a fit to simulated tracks, with strong restrictions on allowed combinations of a, b, c, d. For Φ and p, we find that they predominantly are determined by the focal plane position x, y, with small improvement of the resolution if dx or dy is included. Θ is predominantly given by dx. This is the expected behavior for a dipole spectrometer.

We then add multiple-scattering effects in the detector, assuming 0.5% radiation length for each plane of the detector. The multiple scattering effects rapidly degenerate the precision of dx and dy, strongly affecting the extraction of Θ. In the next step, we also enable multiple-scattering in the target, assuming 1 μm tantalum target.

Simulating the detector response for events from a suitable A' generator, we can simulate the full chain from A' production, track propagation through the spectrometer, detection,

and reconstruction of track parameters at the vertex from the detector measurements. Using this track information, we can then form the invariant mass of the coincidence tracks to find a realistic mass resolution. For the 45 MeV setup, we find mass resolutions around 150 keV and for 55 MeV, a resolution around 170 keV, while the two 31 MeV settings are slightly better with around 120 keV. The natural decay line width of the A' is $\mathrm{O}(1/3 \cdot \alpha\epsilon^2 m_{A'})$, i.e. the observed line width is completely dominated by the spectrometer resolution.

3.2.   Expected count rates

In first order, the signal and irreducible QED background processes are described by the Feynman graphs depicted in Fig. 3.1.

We estimate count rates for A' signal and irreducible QED background using the Mainz generator.

The high luminosity leads to additional background from random coincidences. In this case, the positron spectrometer detects a positron from the irreducible QED background, however the corresponding electron has kinematics that are not detected by the electron spectrometer – the expected rate for this to occur is significantly higher and typically in the tens of kHz. The coincidence condition is then fulfilled with a second scattering reaction in the same time window, producing an electron in the electron spectrometer acceptance. The dominant process here is elastic scattering with initial- or final-state radiation. The corresponding rates were estimated via the OLYMPUS generator.

For coincidences times longer than the bunch spacing, the time window is given by the time resolution of the spectrometers. When individual bunches are resolved, however, a further increase in time resolution has no benefit, as all scattering events from one bunch essentially happens at the same time – the bunch length is too short to resolve below that. For the rate estimate, we assume that we can resolve the 650MHz bunch frequency, requiring timing resolution of $\mathrm{O}(0.5\mathrm{ns})$.

Table 3.1 gives the expected background rates for the two setups at 31 MeV beam momentum, aiming at a A' mass of 13 MeV (13@31) and 17 MeV (17@31), as well as two settings aimed at 17 MeV with possible future beam energies of 45 MeV (17@45) and 55 MeV
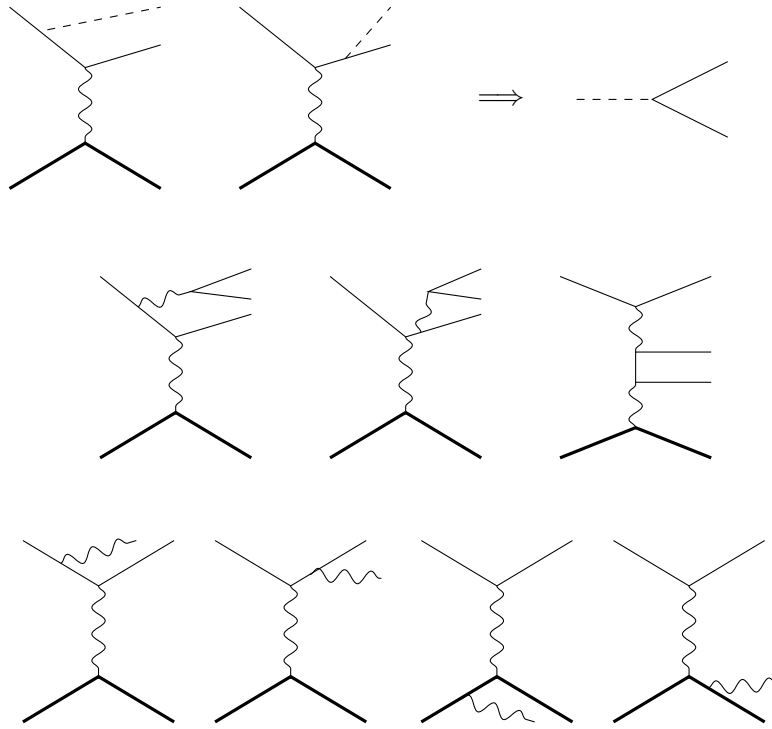
FIG. 3.1: Feynman graphs for the signal and dominant background processes. First row: The A' is produced off the incoming or outgoing lepton and then decays into an e^+e^- pair. Second row: The irreducible QED background processes produce an e^+e^- pair via an intermediate virtual photon. Third row: The trigger condition can be fulfilled by accidental coincidences of an electron from radiative elastic scattering combined with a positron of the irreducible QED background. For the proposed kinematics and luminosity, this is the dominant background process.

(17@55). As can be seen, for the proposed kinematics and beam conditions, the random coincidence background dominates. It is important to note that this background scales with $\mathcal{L}^2$. The figure of merit (FOM) is given by the number of signal events divided by the square root of the background events. Thus, for luminosities in which the accidental coincidence background dominates, the FOM is independent of $\mathcal{L}$ and only scales with the measurement time. The reach cannot be improved with a further increase in instantaneous luminosity.

In Appendix B, the backgrounds generated by the beam interaction with the target are

TABLE 3.1: Background rates for the proposed settings.

Setup	Irreducible QED	Singles e^+	Singles e^-	Random coinc.
13@31	9.1 Hz	30.2 kHz	3.6 MHz	168 Hz
17@31	0.83 Hz	18.2 kHz	751 kHz	21 Hz
17@45	11.2 Hz	32.3 kHz	2 MHz	98 Hz
17@55	71.4 Hz	45.1 kHz	8.5 MHz	589 Hz

discussed.

3.3.   Spectrometer angle dependence

The count rates determined as in the previous section can be used to estimate the sensitivity of the experiment to an A' as a function of the angles of the two spectrometer arms. The sensitivity, defined as

$$\mathcal{S} = \sqrt{2((s+b)\ln(1+s/b) - s)} \qquad (3.3.1)$$

for a background prediction b with no uncertainty, is shown in Figure 3.2 for 1000 hours of run time at 150 μA current and 30 MeV beam energy with a target A' of mass 13 MeV and $\epsilon^2 = $1e-3.

The ideal angle between the two spectrometers is roughly fixed by the kinematics of the A' decay, but an orientation with the positron spectrometer near the beamline and the electron spectrometer farther away is favoured due to the relative reduction in random scattering backgrounds.

Changing either the beam energy or the target A' mass changes the kinematically favoured region. Figure 3.3 shows the same optimisation for an A' of 17 MeV mass at (a) a 30 GeV beam and (b) a 50 GeV beam. This illustrates how useful moveable spectrometer locations would be for the experiment.
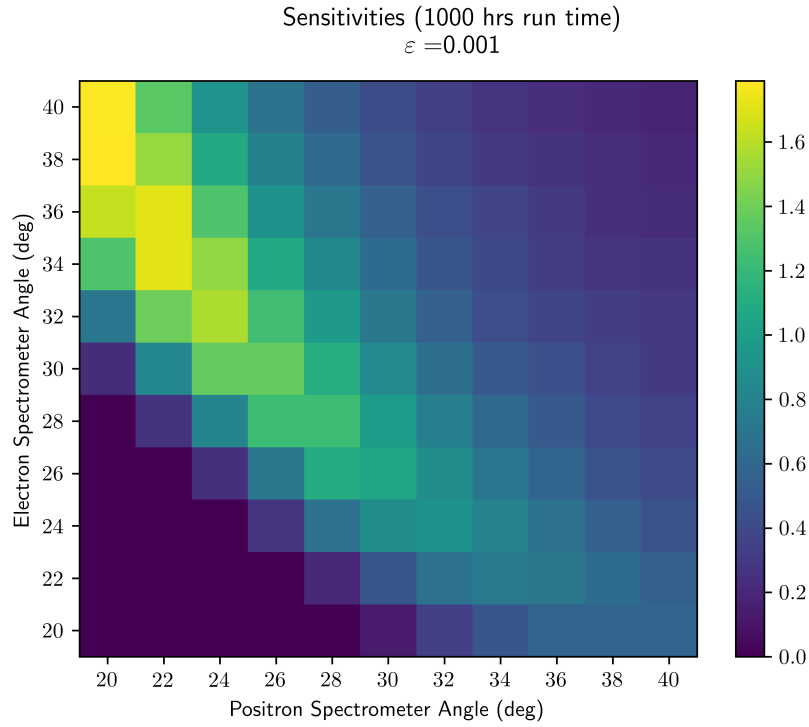
FIG. 3.2: Projected sensitivity as a function of electron and positron spectrometer angles from the beamline for a 13 MeV A' with a beam energy of 30 MeV.

(a) 30 MeV beam   (b) 50 MeV beam
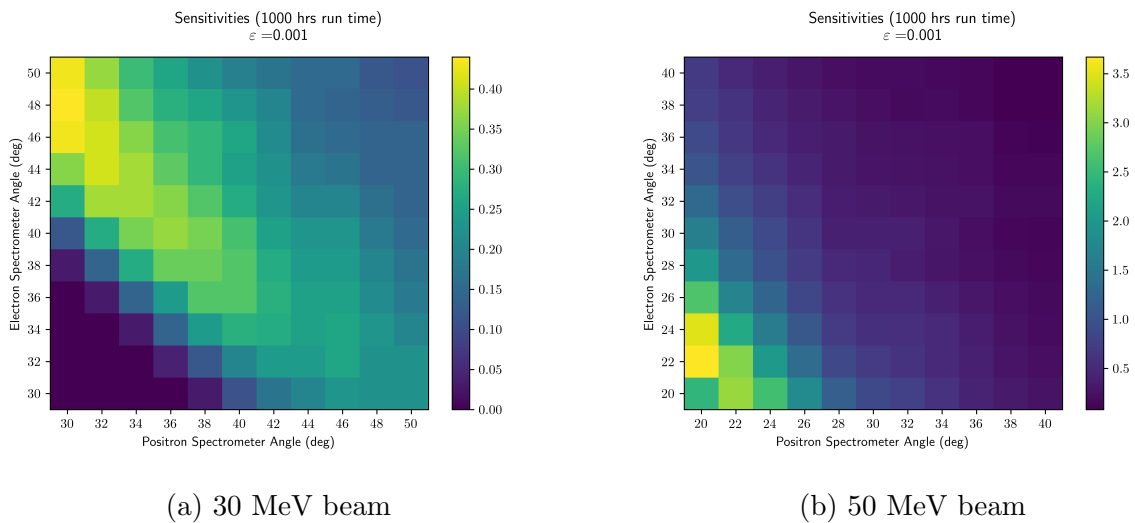
FIG. 3.3: Sensitivity to a 17 MeV A' as a function of spectrometer angle for 30 and 50 MeV beam energies.

3.4.   Projected sensitivity

The acceptance of the experiment dominate the background signal shapes, making the irreducible background and random coincidences similar. We therefore estimate the total background by scaling up the irreducible background according to the expected rates. The reach is calculated by integrating the background over the expected signal width ($\pm 1.7\sigma$), and calculating ϵ^2 so that the signal would be bigger than a 2σ fluctuation of the background. Figure 3.4 shows the signal on top of the anticipated background for the 13@31 setting for $\epsilon^2 = 10^{-3}$.
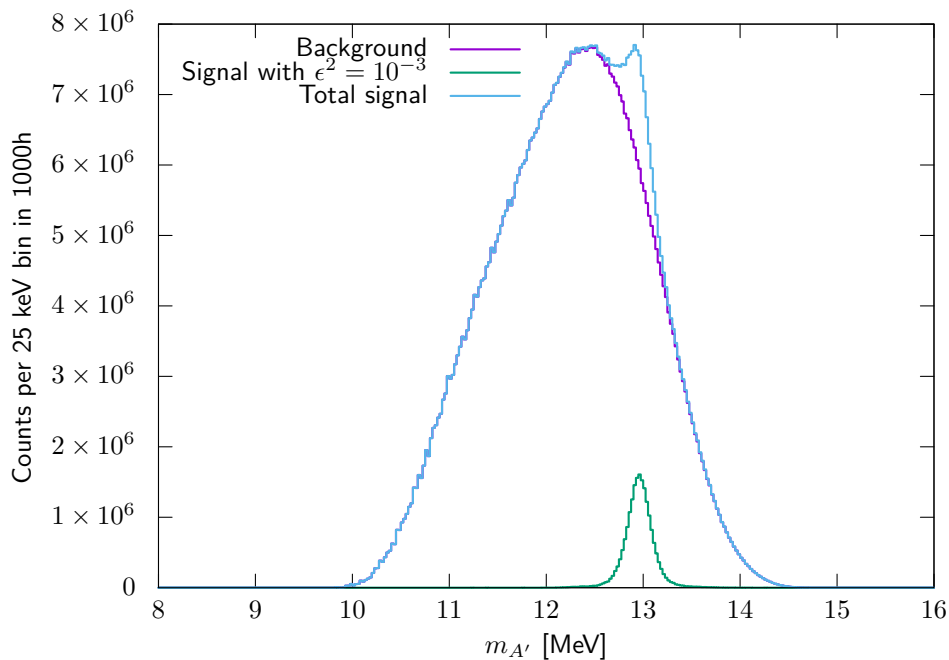

FIG. 3.4: Expected background, signal and total rate as a function of invariant mass for the 13@31 MeV setting, calculated for a $m_{A'}$ mass of 13 MeV. To make the signal visible with the naked eye, a rather larger coupling of $\epsilon^2 = 10^{-3}$ was assumed.

Note that for smaller ϵ^2, the background and total signal are visually indistinguishable. However, the statistical uncertainty in the measured background becomes very small, and deviations are still detectable if the shape of the background below the peak is understood.

Since random coincidences dominate the background, the pure random background will be very accurately measured by the experiment itself by mixing electron and positron spec-

trometer data from different events. This mixing destroys all correlations between the spectrometers, generating a pure sample of the random coincidences. Since, in principle, every combination of events $i \neq j$ can be used, the statistics grows quadratically with the recorded number of events.

Figures 3.5 and 3.6 show the achievable reach for the four settings assuming 1000h beam-time each.
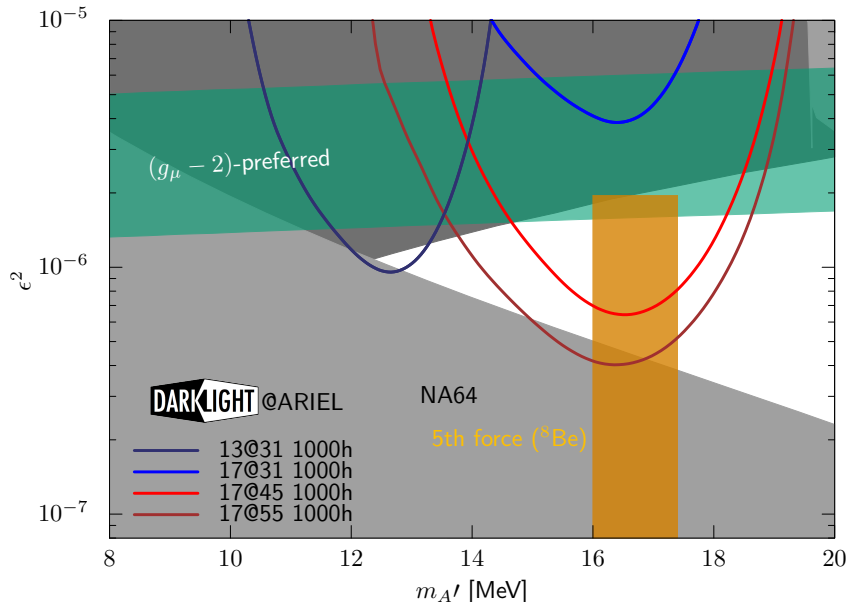

FIG. 3.5: The projected reaches on a linear plot for three separate 1000 h data taking runs: 13@31 (dark blue); 17@31 (light blue); 17@45 (light red); 17@55 (dark red). Light gray areas are excluded by other experiments sensitive to a lepton coupling. The dark gray area is excluded by electron g-2 only.

Using a beam energy of 30 MeV and the optimal spectrometer angles and central e^+ and e^- momenta for a 13 MeV A', exclusion limits were set on ϵ^2 at 95% confidence level as a function of $m_{A'}$. The CLs test statistic is used. Two limits are shown in Figure 3.7: one assuming a background uncertainty of $\sqrt{n}$ and one with a very small background uncertainty (10 events, regardless of bin content). The true background uncertainty is expected to be small due to the event-mixing background prediction method available, but systematic uncertainties will inevitably be present. This figure serves to illustrate the variability in sensitivity for low and high extremes of the uncertainty.
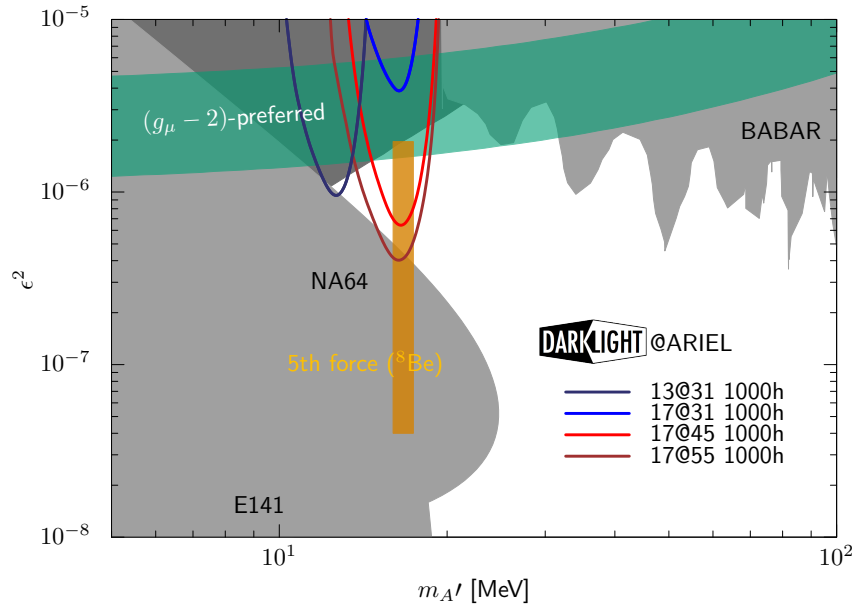
FIG. 3.6: The projected reaches on a logarithmic plot for three separate 1000 h data taking runs: 13@31 (dark blue); 17@31 (light blue); 17@45 (light red); 17@55 (dark red) . Light gray areas are excluded by other experiments sensitive to a lepton coupling. The dark gray area is excluded by electron g-2 only.
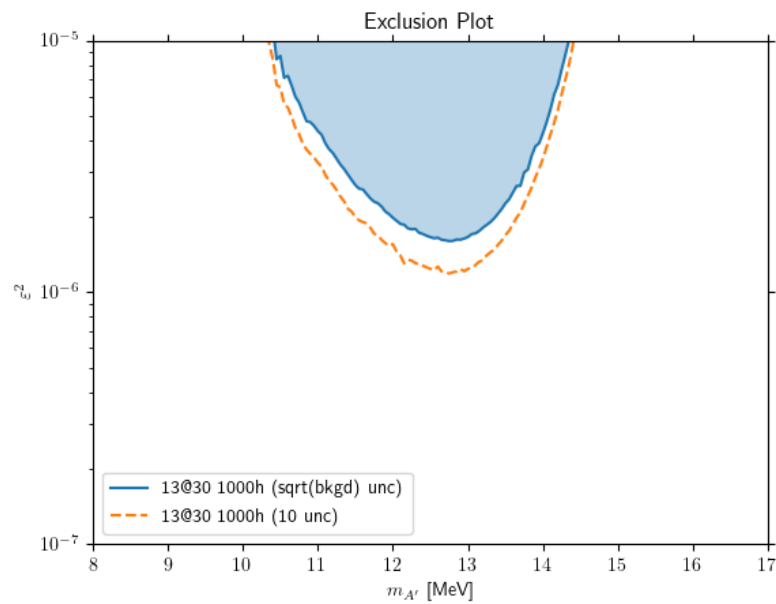

FIG. 3.7: 95% CL exclusion limits

4. SCHEDULE

We expect to be ready to begin commissioning within about twelve months after funding becomes available. Table 4.1 shows the milestones associated with the anticipated schedule

TABLE 4.1: Estimated schedule for the proposed experiment.

Milestone		Date
Proposal submitted		March 2021
Proposal approved		April 2021
Canadian groups funded		April 2022
Test A: use existing target		August 2022
	Test foils	
	Measure radiation	
	Use calibrated radiation monitors	
	to verify simulations	
Technical design of experiment completed		August 2022
Technical review by TRIUMF		September 2022
US groups funded		October 2022
Construction of experiment begins		October 2022
Safety protocols established		December 2022
Test B: experiment at beam dump		April 2023
	Install quads	
	Install target and existing spectrometer	
	Run 10-30 MeV, 100 μA	
	Measure elastic Møller scattering	
	Test trigger scintillators, GEMS	
Construction of experiment completed		October 2023
Experiment installed		November 2023
Data taking begins		April 2024
Data taking completed		September 2024

5. DARKLIGHT COLLABORATION

The DarkLight collaboration consists of five institutions each from Canada and the U.S., and the membership is listed as follows:

R. Alarcon, R. Dipert, G. Randall
Arizona State University, Tempe, AZ

A. Christopher, T. Gautam, M. Kohl, J. Nazeer, T. Patel, M. Rathnayake, M. Suresh
Hampton University, Hampton, VA

S. Benson
Thomas Jefferson National Accelerator Facility, Newport News, VA

J. Bessuille, P. Fisher, D. Hasell, E. Ihloff, R. Johnston, J. Kelsey, I. Korover,
S. Lee, X. Li, R. Milner, M. Moore, P. Moran, C. Vidal, Y. Wang
Laboratory for Nuclear Science, MIT, Cambridge, MA

R. Kanungo
Saint Mary's University, Halifax, Canada

J. C. Bernauer[48], E. Cline, R. Corliss, K. Dehmelt, A. Deshpande
CFNS, Stony Brook University, Stony Brook, NY

R. Baartman, O. Kester, R. Laxdal, A. Mahon, K. Pachal, T. Planche, S. Yen
TRIUMF, Vancouver, Canada

M. Hasinoff
University of British Columbia, Vancouver, Canada

W. Deconinck
University of Manitoba, Winnipeg, Canada

J. Martin
University of Winnipeg, Winnipeg, Canada

Co-Spokespeople: Jan Bernauer, Ross Corliss, and Richard Milner

6. INSTITUTIONAL RESPONSIBILITIES

The major tasks involved in the proposed experiment are listed in Table 6.1. The magnetic spectrometers, target system, and scattering chamber with vacuum system and controls will be the primary responsibility of the MIT group. The GEM detectors and GEM readout will be carried out by the Hampton University group. Stony Brook University will take care of the data acquisition and slow control system. A consortium of Canadian institutions (Saint Mary's University, TRIUMF, University of British Columbia, University of Manitoba, and University of Winnipeg will design, construct, and provide readout electronics for the trigger hodoscopes and take care of integration with the ARIEL machine.

7. BUDGET

The estimated funds to construct the equipment, including spectrometers, target chamber, detectors and electronics are costed in Table 7.1 and total 310,000 USD. Funding at Hampton University for the GEMS existed from the NSF Phase-1 MRI award and was used to produce eight triple-GEMs. While they are partially committed elsewhere presently, there are sufficient GEMs to mount this experiment.

Appendix A: Details on GEM construction

1. Single-mask technique

The need to routinely construct large-area GEM detectors with reproducible gain has been met by adopting the single-mask technique to produce GEM foils. Previously, the size of GEM foils with the standard double-mask technique had been limited due to accumulative misalignment of the two opposing photo masks. Problems resulted in the non-central regions where the hole geometry was increasingly deformed, resulting in gain non-uniformity and inefficiency.

With the single-mask technique, a hole alignment is no longer required, and largely uniform gains have been achieved. Figure A.1 shows a comparison of the two schemes. The key step has been the electro-etching of the bottom copper layer with galvanic protection of the top

TABLE 6.1: Major tasks and responsibilities for the proposed experiment.

Task	Lead Group
Magnetic spectrometers	MIT
design and construction	
ray tracing and simulation	
field mapping at TRIUMF	
Target and Scattering Chamber	MIT
design and construction	
vacuum system and controls	
GEM detectors	Hampton U
design and construction	
readout electronics	
Data Acquisition	Stony Brook U.
slow controls	
integration	
software	
Trigger hodoscopes	TRIUMF, UBC, UM, UW, and SMU
design and construction	
readout electronics	
Integration with ARIEL	TRIUMF, UofM
vacuum system	
beam diagnostics, bunch clock, and controls	

layer. The CERN workshop is now able to routinely produce high-quality GEM foils of up to 2 m in length. The maximum size is only limited by the machines hosting the chemical etching bath.

TABLE 7.1: Estimated budget for the proposed experiment.

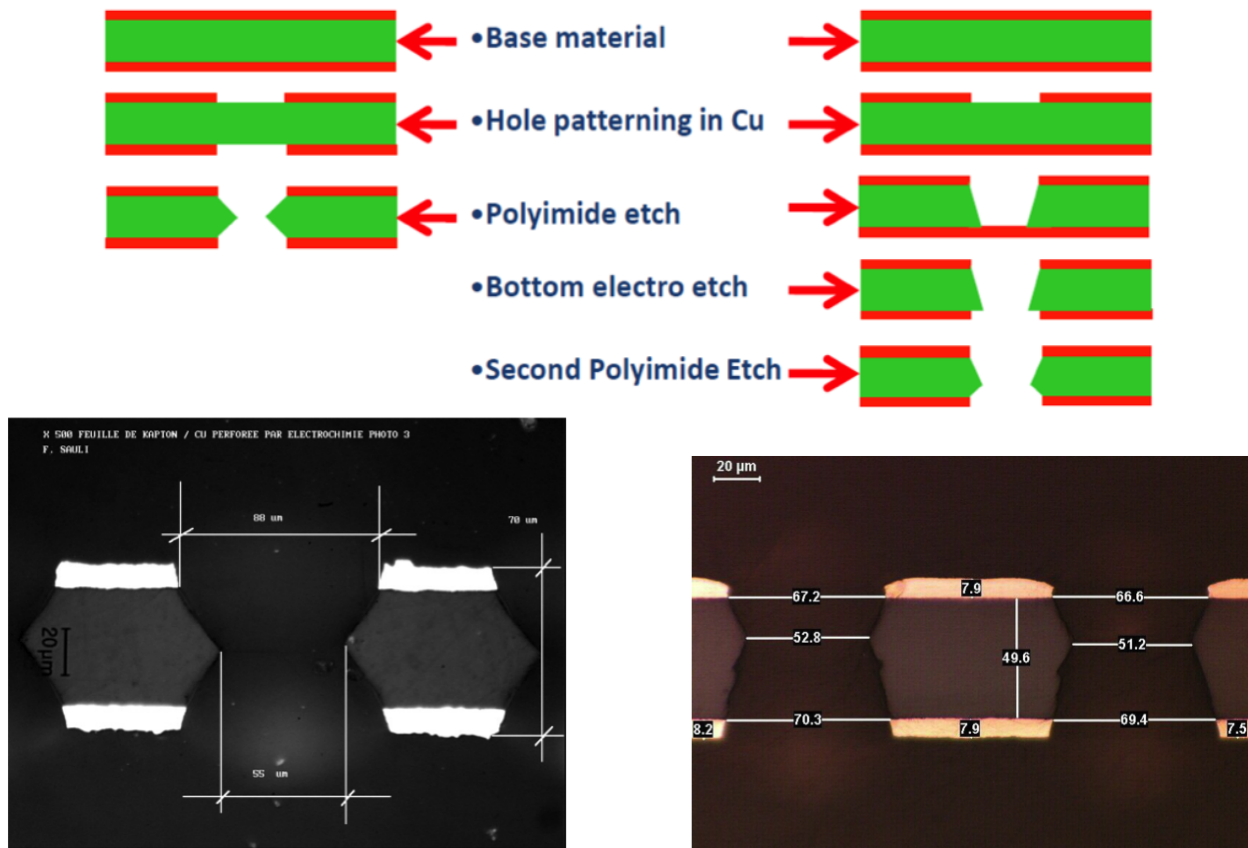| Item	Cost (kUSD)
Spectrometers	165
Target chamber	50
GEMs	30
Scintillator	20
Electronics	45
Total	310

FIG. A.1: Left: Double-mask etching technique. Right: Single-mask technique.

2.   NS2 Concept

A novel technique called NS2 ("No Stretch-No Stress") has been adopted to assemble the detectors. This consists of a mechanical system to stretch the foils, which avoids the conven-

tional gluing of the foils to frames and allows the foils to be stretched with greater tension than with the foil-on-frame gluing technique. Subsequently, no spacer grid is required, eliminating dead areas and improving the gas flow inside the chamber. This design has been developed at CERN in the context of the CMS upgrade at LHC. For that project, a large number of large-area GEM detectors in trapezoidal geometry, ~ 1.5 m long elements for the forward muon endcap have been under construction at CERN.
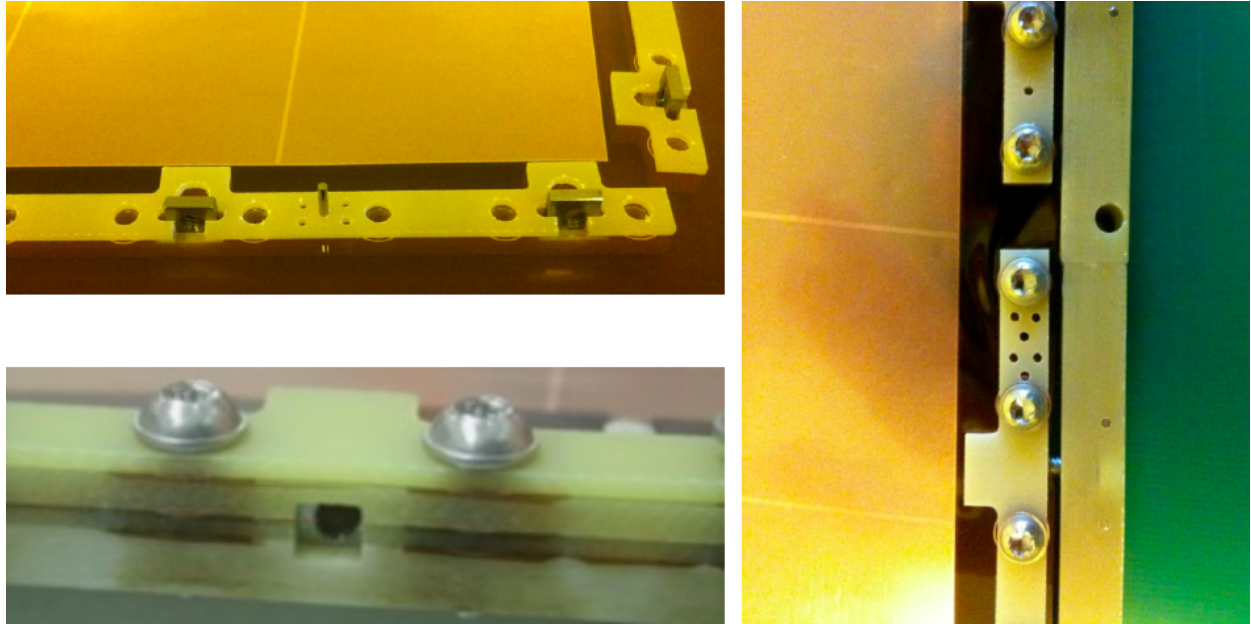

FIG. A.2: Photographs of the CMS NS2 frames at CERN. Upper left: single layer of the inner frame showing a groove with an embedded nut to hold the stretching screw. Lower left: Bolted inner frame stack to clamp all layers, showing the hole with the embedded nut for the stretching screw. Right: Inner frame stack with horizontal screws through the outer frame for stretching. The gap between inner and outer frame is a few mm to accommodate the tension.

The GEM detectors constructed for the proposed experiment were based on the CMS design, but modified to minimize material in the active area. The inner stack consists of five layers, Drift, 3x GEM, and Readout, which are clamped together by inner frame parts (see Fig. A.2). The inner frames contain embedded nuts in horizontal orientation that allow them to be bolted and stretched through a stiff outer frame, which is large enough to avoid any deformation. Figure A.3 shows a schematic view of the double-frame structure with the clamped inner stack of the GEMs for DarkLight Phase 1c.
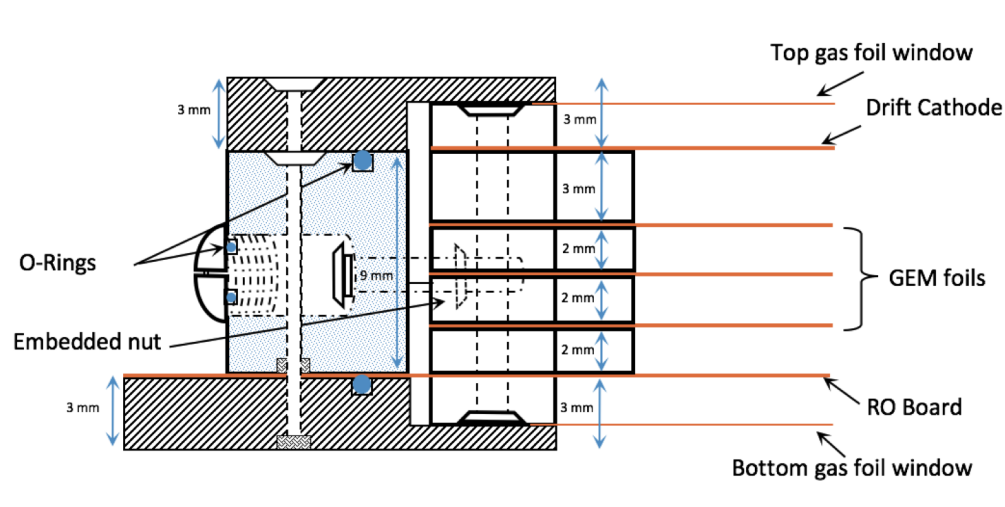
FIG. A.3: Schematic view of the NS2 double frame mechanical system to provide
simultaneous stretching of a clamped stack of foils.

This structure is sandwiched between a top and bottom lid with thin chromium coated
Kapton windows. The lid frames are bolted to the outer frame and O-ring sealed.
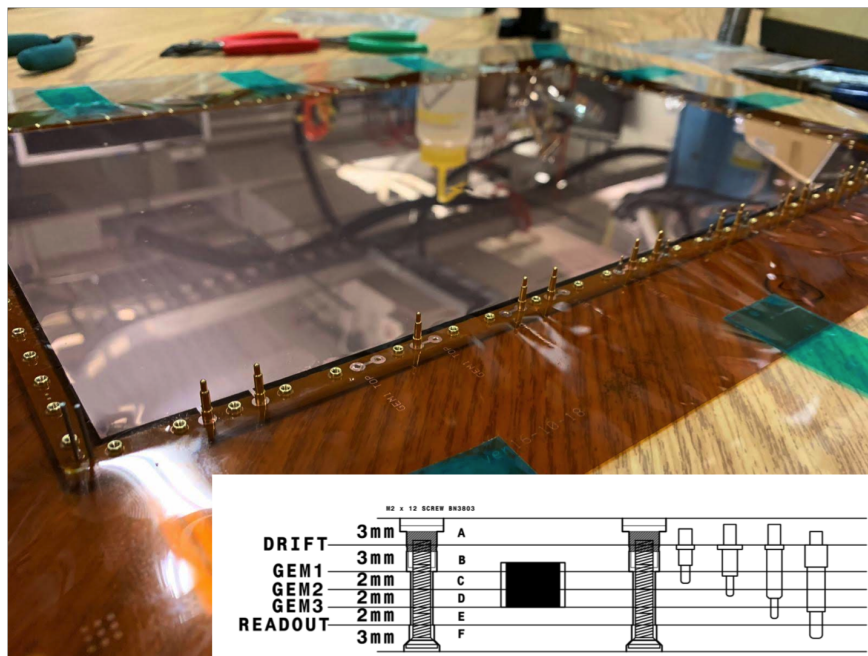

FIG. A.4: Photo of the drift foil layer with spring loaded high-voltage pins to distribute
the voltages picked up from the readout board to each GEM foil layer.

The Readout layer extends beyond the sealed gas volume out to the exterior, in order to
interface with the readout electronics and to supply high voltage. Standard-CERN ceramic

low-impedance passive voltage dividers are used. The individual voltages are guided through the inner frame stack to each respective layer, with spring-loaded pins, as indicated in Fig. A.4. The GEM foils have been segmented into ten sectors, with an SMD resistor at the entrance to each pad for protection against shorts. Figure A.5 shows photos of the realized GEM detector: of the inner frame stack before stretching (left), and with the main frame surrounding the inner stack and after stretching (right).
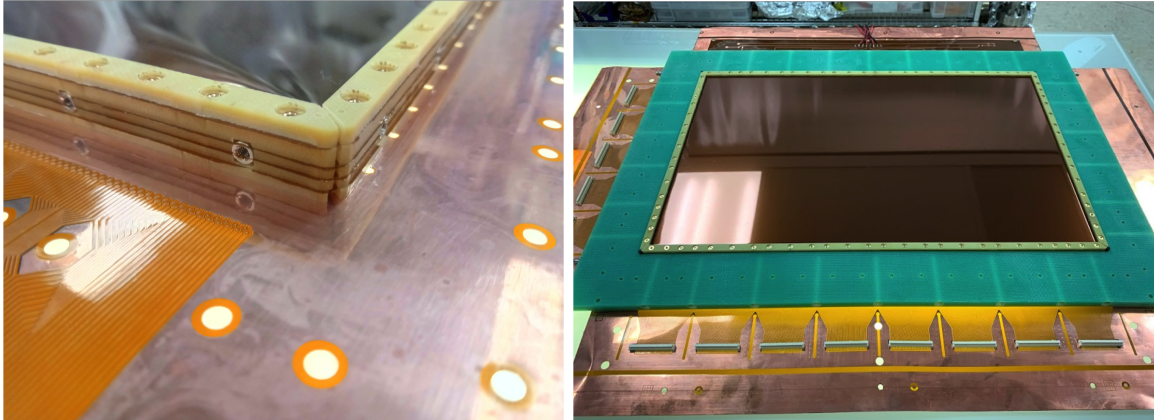

FIG. A.5: Left: Inner frame stack after trimming excess foils and before stretching. The embedded nut for stretching can be seen. Right: View of the GEM detector after stretching with screws inserted through the rigid outer main frame.

3.   Readout

The readout chain of the GEM setup is based on Analog Pipeline Voltage (APV) chips and Multi-Purpose Digitizers (MPDs), which were acquired for a total of eight chambers.

APV backplanes (Fig. A.6) feed the operating low voltage to the APV chips and provide digital and analog connections to the MPD. One MPD can process up to 16 APVs in four groups of four. With the latest MPD firmware version 4 allowing fast VME modes as well as optical readout only up to 15 APVs can be connected. In the realized design, each GEM chamber (13 APVs) is read out with one MPD.

The fast VME readout mode was implemented in the DAQ software, the readout time for 13 APVs of one GEM was reduced from about 1 ms in BLT mode (32-bit block transfer) to now < 200 μs in 2eSST mode (64-bit block transfer).
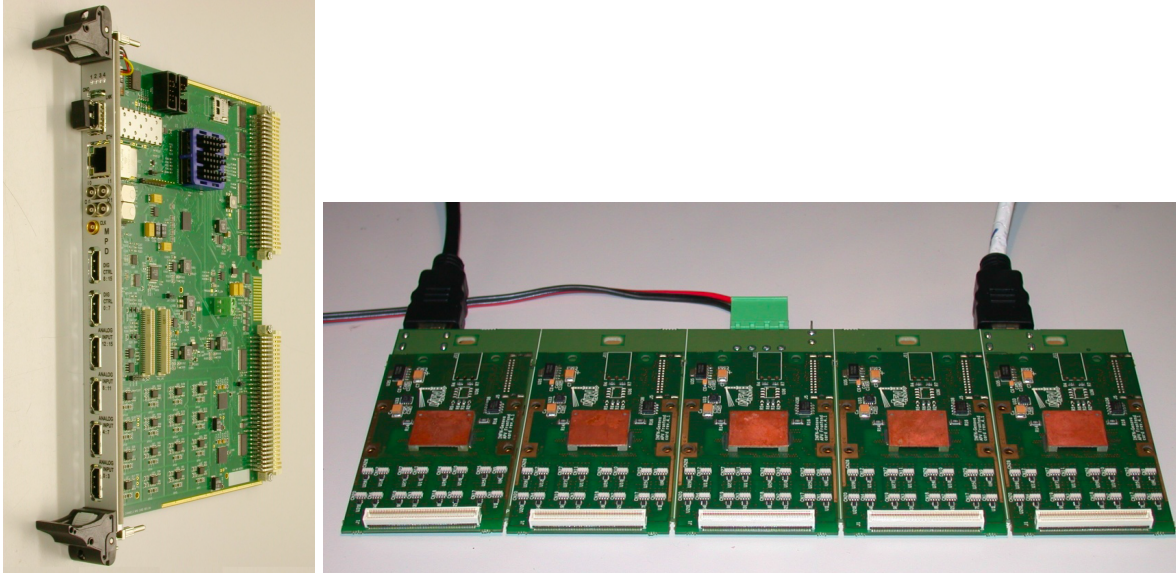
FIG. A.6: Left: MPD4 VME module. Right: 5-slot APV backplane equipped with APV front-end v4.1.

Figure A.7 shows a stack of two assembled GEM elements fully equipped with APV frontend electronics, backplanes, analog and digital patch panels, and low-voltage regulator board.
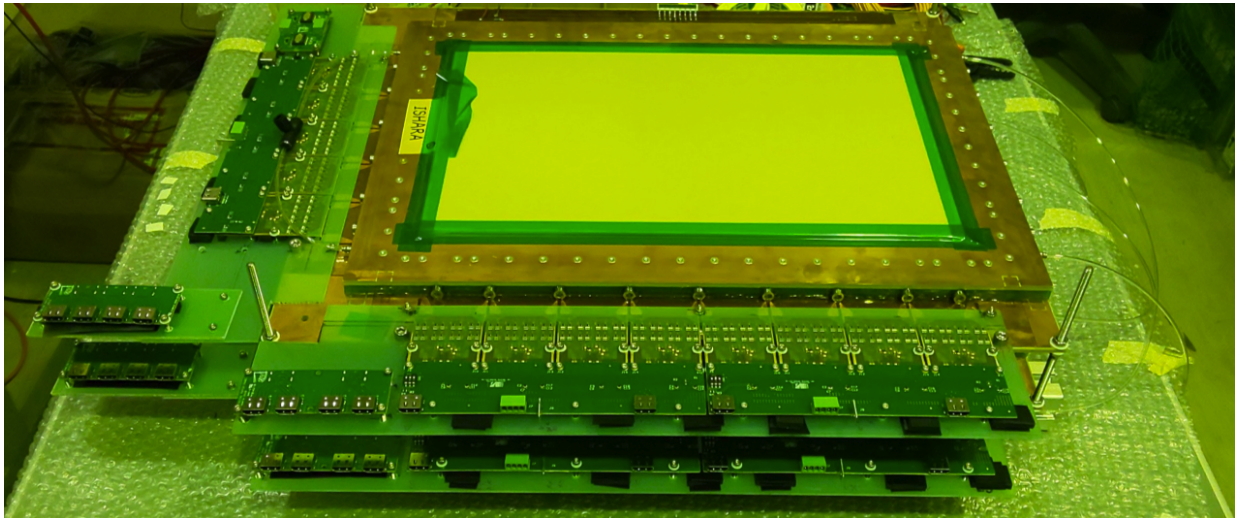

FIG. A.7: Photo of two assembled GEM elements fully equipped with APV frontend electronics, backplanes, adapter boards and low-voltage regulator board.

Figure A.8 shows two plots of the distribution of clusters observed with one GEM element (40 cm wide and 25 cm tall) in a recent test beam experiment at ELPH at Tohoku University

in Sendai on December 16-17, 2019. The left figure was obtained for a focused beam of ≈ 700 MeV positrons at a few kHz, the right figure after defocusing the beam with a 10 mm lead sheet 4 m upstream of the GEM element.
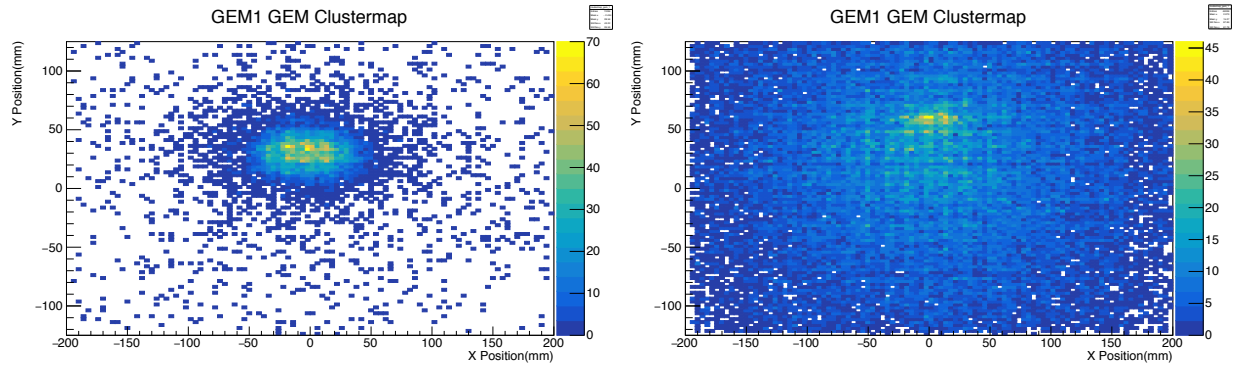

FIG. A.8: Distribution of detected clusters with one new 25×40 cm^2 GEM element in the ELPH test beam with focused beam (left) and defocused beam (right).

Appendix B: Beam Heating of Target Foil

Temperature Distribution in a Radiation-Cooled Target Foil Traversed by a Gaussian Beam

C. Tschalär

November 7, 2017

1 Description

A thin target foil penetrated by a particle beam of circular cross section much smaller than the width of the foil dissipates the deposited beam power by radial heat conduction and radiation off both foil surfaces. We calculate the radial temperature distribution for a Gaussian beam spot of r.m.s. radius r_0.

2 Heat Transport Equations

The radial power gradient dP/dr generated by the beam power deposition, heat conduction, and radiation is

$$-\frac{dP}{dr} = -P_0 \frac{2r}{r_0^2} e^{-r^2/r_0^2} + 4\pi r \sigma \epsilon (T^4 - T_m^4) = 2\pi \lambda t \frac{d}{dr}\left[r\frac{dT}{dr}\right] = 2\pi \lambda t \left[r\frac{d^2T}{dr^2} + \frac{dT}{dr}\right] \quad (1)$$

where
P_0 = total beam power deposition,
$\sigma = 5.67 \cdot 10^{-12} W/(cm^2 K^o)$ is the Stefan-Boltzmann constant,
ϵ is the total emissivity of the foil,
T_m the ambient temperature,
λ the thermal conductivity of the foil, and
t the thickness of the foil.
If we define

$$\rho \equiv r\sqrt{\frac{4\pi\sigma\epsilon T_m^4}{2\pi\lambda t T_m}}; \quad \omega \equiv \frac{P}{2\pi\lambda t T_m}; \quad \tau \equiv T/T_m; \quad \Omega \equiv \frac{P_0}{\pi\lambda t T_m \rho_0^2} e^{-\rho^2/\rho_0^2} , \quad (2)$$

we find the relations

$$\omega = -\rho\frac{d\tau}{d\rho}; \quad \rho(\tau^4 - 1 - \Omega) = -\frac{d\omega}{d\rho} \quad (3)$$

1

and

$$\rho^2 \frac{d^2\tau}{d\rho^2} + \rho \frac{d\tau}{d\rho} + \rho^2(\tau^4 - 1) = 0 \ . \tag{4}$$

For radii much larger than the beam spot, Ω vanishes, τ approaches unity, and $(\tau - 1)$ may be approximated by 4ν where $\nu \equiv \tau - 1$ so that, for $\nu \ll 1$,

$$\rho^2 \frac{d^2\nu}{d\rho^2} + \rho \frac{d\nu}{d\rho} + 4\rho^2\nu = 0 \tag{5}$$

and $\nu(\rho)$ is proportional to $K_0(2\rho)$, a Hyperbolic Bessel function of order zero. We define a proportionality factor A by

$$\nu(\rho) \equiv A \cdot \frac{2}{\sqrt{\pi}} K_0(2\rho) \ . \tag{6}$$

Correspondingly, $\omega(\rho)$ is

$$\omega(\rho) = -\rho \frac{d\nu}{d\rho} = A \frac{4}{\sqrt{\pi}} \rho K_1(2\rho) \tag{7}$$

where K_1 is a Modified Bessel function of order 1. Both solutions satisfy the boundary condition at $\rho \to \infty$ where $\omega \to 0$ and $\tau \to 1$. The factor A is determined by the total beam power P_0 deposited in the target foil.
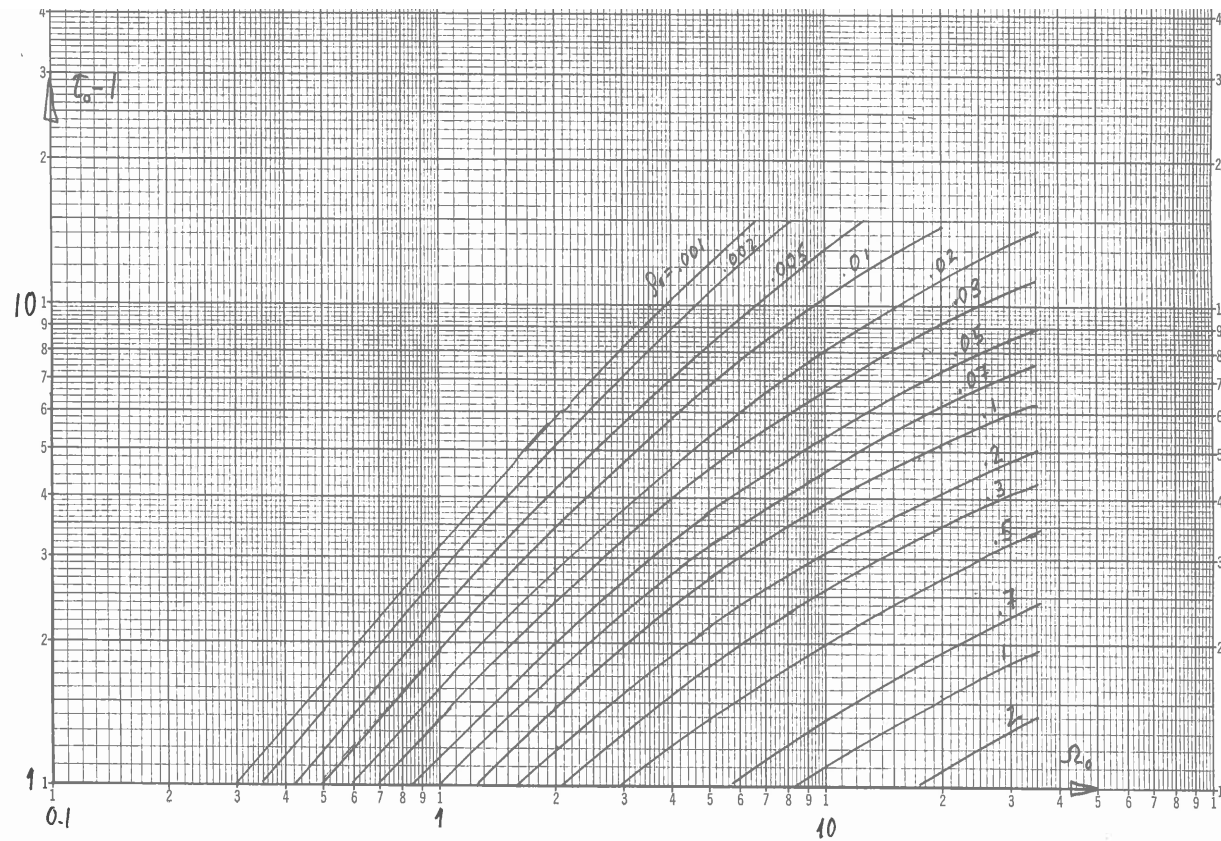
3   Numerical Solution

Using approximations (6) and (7) as starting values at an appropriately large value of ρ_ν, the coupled equations (3) may be integrated numerically to $\rho = 0$ where ω is required to reach zero. The latter condition dictates the choice of the factor A for a given value of Ω_0 where

$$\Omega_0 \equiv \frac{P_0}{\pi \lambda t T_m}; \qquad \rho_0 \equiv r_0 \sqrt{\frac{2\sigma\epsilon T_m^3}{\lambda t}} \ . \tag{8}$$

The resulting values of $\tau_0 - 1 = (T_0 - T_m)/T_m$, where T_0 is the foil temperature at the beam center, are plotted in Fig. 1 as functions of Ω_0 for a set of values ρ_0. The FORTRAN routine used in these calculations is listed in Fig. 2.

Figure 1: τ_0 as a function of Ω_0 for various values of ρ_0

```
         REAL*8 T,TN,T1,OM,OMN,OM1,R,RN,A,DR,P,PN,ON,RON,E
10       READ(5,100) TN,OMN,RN
100      FORMAT(4F12.9)
20       READ(5,101) L,N,ON,RON
101      FORMAT(2I6,2F12.9)
         DR=RN/FLOAT(L*N)
         PN=ON/RON**2
30       READ(5,100) A
         T=(TN-1.D0)*A+1.D0
         OM=OMN*A
         R=RN
         DO 1  M=1,L
         DO 2  I=1,N
         E=MIN(R/RON,5.D0)
         P=PN*DEXP(-E**2)
         T1=T+DR*(OM/R+0.5D0*DR*(T**4-1.D0-P-OM/(R**2)))
         OM1=OM+DR*(R*(T**4-1.D0-P)+0.5D0*DR*(4.D0*OM*T**3+T**4-1.D0-P))
         R=R-DR
         T=T1
         OM=OM1
2        CONTINUE
         WRITE (6,200) R,T,OM
200      FORMAT(4F12.9)
         IF(OM) 60,60,1
1        CONTINUE
60       READ(5,101) J
         IF(J) 40,30,20
40       READ(5,101) K
         IF(K) 10,10,50
50       END
```

Figure 2: FORTRAN program to integrate eqns. (3)

[1] *Foundations of Nuclear and Particle Physics*, T.W. Donnelly, J. Formaggio, B.R. Holstein, R.G. Milner and B. Surrow, Cambridge University Press, 2017.

[2] A. Krasznahorkay *et al.*, Phys. Rev. Lett. **116**, 042501 (2016).

[3] A. Krasznahorkay *et al.*, Acta Physica Polonica B, **50**, 675.

[4] A. Krasznahorkay *et al.*, arXiv: 1910.10459, October 23, 2019.

[5] F. Zwicky, Helvetica Physics Acta **6**, 110 (1933).

[6] G.W. Bennett *et al.* (Muon g-2 Collaboration), Phys. Rev. D **73**, 072003 (2006).

[7] M. Freytsis, G. Ovanesyan, and J. Thaler, Jour. High Energy Physics, **2010**, 111 (2010).

[8] D. Banerjee *et al.* [NA64], Phys. Rev. D **101**, 071101 (2020).

[9] *Has a Hungarian physics lab found a fifth force of Nature?*, **Nature News**, 25 May 2016.

[10] See https://www.cnn.com/2019/11/22/world/fifth-force-of-nature-scn-trnd/index.html https://www.independent.co.uk/news/science/dark-matter-particle-hungary-atomki-nuclear-research-force-nature-a9210741.html?amp

[11] I. Counts *et al.*, arXiv:2004.11383, April 2020.

[12] J. Feng *et al.*, Phys. Rev. Lett. **117**, 071803 (2016).

[13] U. Ellwanger and S. Moretti, arXiv:1609.01669.

[14] D.S.M. Alves and N. Weiner, JHEP 1807, 092 (2017).

[15] L. Delle Rose *et al.* arXiv: 1905.05031.

[16] L. Delle Rose *et al.* Front. in Phys. **7**, 73 (2019).

[17] X. Zhang and G.A. Miller, Phys. Lett. B**773**, 159 (2017).

[18] A. Aleksejevs *et al.*, arXiv:2102.01127.

[19] P. Kalman and T. Kaszthelyi, arXiv:2005.10643.

[20] See https://theory.fnal.gov/events/event/first-results-from-the-muon-g-2-experiment-at-fermilab/

[21] I. Bediaga *et al.*, arxiv:1808.08865, April 2019.

[22] T. Åkesson *et al.*, arxiv:1808.05219, August 2018.

[23] A. Berlin *et al.*, Phys. Rev. D**99**, 075001 (2019).

[24] K. Ban *et al.*, arxiv:2012.04190, March 2021.

[25] L. Doria *et al.*, arxiv:1809.07168, September 2018.

[26] N. Gninenko *et al.*, arXiv:2003.07257.

[27] G. Piperno *et al.*, arxiv:2002.11671, February 2020.

[28] D. Banerjee *et al.* [NA64], Phys. Rev. Lett. **120**, 231802 (2018).

[29] D. Banerjee *et al.* [NA64], Phys. Rev. D **101**, 071101 (2020).

[30] T. Beranek, H. Merkel, and M. Vanderhaeghen, Phys. Rev. D **88** 015032 (2013).

[31] B. S. Henderson *et al.* [OLYMPUS], Phys. Rev. Lett. **118**, no.9, 092501 (2017).

[32] ESTAR program, NIST.

[33] D. Goosman, *Monte Carlo 20 and 45 MeV Bremsstrahlung and Dose-Reduction Calculations*, Proceedings of the 16th International Congress on High Speed Photography and Photons, 1984, Strasbourg, France.

[34] X. Mao, K.R. Kase, and W.R. Nelson, *Giant Dipole Resonance Neutron Yields Produced by Electrons as a Function of Target Material and Thickness*, SLAC-PUB-6628, January 1996.

[35] J.C. Liu, W.R. Nelson, K.R. Kase, and X.S. Mao, *Calculations of the Giant-Dipole Resonance Photoneutrons using a Coupled EGS4-Morse Code*, SLAC-PUB-95-6764, October 1995.

[36] Y. Tsai, Rev. Mod. Phys. **46**, 815 (1974).

[37] R.D. Evans, *The Atomic Nucleus*, Mc-Graw-Hill, New York (1955).

[38] M. Tanabashi *et al.*. (Particle Data Group), Phys. Rev. D **98**, 030001 (2018) and 2019 update.

[39] R. Alarcon *et al.*, Phys. Rev. Lett. **111**, 164801 (2013).

[40] C. Tschalär *et al.*, Nucl. Instr. and Meth. A **729**, 69 (2013).

[41] R. Alarcon *et al.*, Nucl. Instr. and Meth. A **729**, 233 (2013).

[42] C.S. Epstein and R.G. Milner, Phys. Rev. D **94**, 033004 (2016).

[43] C.S. Epstein *et al.* (The DarkLight Collaboration), Phys. Rev. D **102**, 012006 (2020).

[44] *Møller Scattering at Low Energy*, Ph.D. thesis, Department of Physics, Massachusetts Institute of Technology, Charles S. Epstein, September 2018.

[45] P. Ilten, Y. Soreq, J. Thaler, M. Williams and W. Xue, Phys. Rev. Lett. **116**, no.25, 251803 (2016) doi:10.1103/PhysRevLett.116.251803 [arXiv:1603.08926 [hep-ph]].

[46] Note1, alternatively, Tungsten can be used, which improves heat conduction but is more brittle. Luminosities and reach are virtually unaffected by such a replacement.

[47] Note2, originally built by the Hampton group for the OLYMPUS experiment through an

NSF/MRI award. These detectors were used in the DarkLight Phase 1a commissioning at the LERF and are also in use at MUSE.

[48] Note3, also with Riken BNL Research Center, Upton, NY.